

Machine Learning insights on the \mathbb{Z}_3 3HDM with Dark Matter

Fernando Abreu de Souza,^{1,*} Rafael Boto,^{2,†} Miguel Crispim Romão,^{3,1,‡} Pedro N. de Figueiredo,^{4,§} and Jorge C. Romão^{4,¶}

¹*LIP – Laboratório de Instrumentação e Física Experimental de Partículas, Escola de Ciências, Campus de Gualtar, Universidade do Minho, 4701-057 Braga, Portugal*

²*Institute for Theoretical Physics, Karlsruhe Institute of Technology, 76128 Karlsruhe, Germany*

³*Institute for Particle Physics Phenomenology, Durham University, Durham DH1 3LE, UK*

⁴*Departamento de Física and CFTP, Instituto Superior Técnico, Universidade de Lisboa, Av Rovisco Pais, 1, P-1049-001 Lisboa, Portugal*

We study a 3-Higgs Doublet Model (3HDM) with an imposed \mathbb{Z}_3 symmetry, allowing for two Inert scalar doublets and one active Higgs doublet. The WIMP dark matter candidates correspond to two mass-degenerate states, H_1 and A_1 , which possess opposite CP quantum numbers and can reproduce the correct relic density simultaneously with all theoretical and experimental constraints. We use state-of-the-art machine learning algorithms to probe the parameter space of the model by employing an Evolutionary Strategy augmented with Novelty Reward. We consider two situations: a limit for the dark matter mixing angle θ that closes a gauge annihilation channel that would deplete the DM relic density, and the general case without imposing this limit. For both scenarios, we find viable dark matter candidates within two separate mass regimes, ranging from $50 \text{ GeV} \leq m_{\text{DM}} \lesssim m_W$ and $380 \lesssim m_{\text{DM}} \lesssim 1000 \text{ GeV}$. Moreover, we find it is possible to fulfill all the existing constraints while still obtaining values for the dark matter-higgs coupling of order $\sim \mathcal{O}(0.1)$.

Exploring the model outside the $\theta = \frac{\pi}{4}$ limit proved to be an extremely challenging task, as there are regions which seem easy to explore when projected on a 2D plane, yet may be completely disconnected on the hypersurface supporting the valid points, given its non-convex and multi-dimensional nature. We consider new methods of prototype selection to seed new exploration runs, which allow for efficient global scans over the parameter space.

I. INTRODUCTION

The Standard Model is our current best description of particle physics. In 2012, yet another of its postulates was proven with the discovery of the 125 GeV Higgs boson, that arises from a scalar doublet field, by the ATLAS [1] and CMS [2] collaborations. Despite the success of the SM, there are still open problems that need to be addressed, such as Dark Matter (DM), which comprises about 85% of all matter in the Universe [3]. Similar to the fermions, the number of bosons must be determined experimentally. Therefore, one may consider a N-Higgs Doublet Models (NHDM) approach to provide suitable DM candidates, by extending the SM with additional scalar doublet fields with a preserved symmetry that stabilizes the DM candidates. Given its elusive nature, DM has yet to be detected directly and experiments place increasingly stringent bounds. The allowed parameter space of minimal extension models, such as the Inert Doublet Model (IDM) [4–7] with a single additional doublet and a \mathbb{Z}_2 symmetry, is thus becoming progressively more limited [8–22]. This motivates the study of larger models, since they provide richer phenomenology and can predict a DM candidate in regions already excluded in simpler models.

In this work, we consider the possibility of a three-Higgs-doublet model (3HDM) with an additional \mathbb{Z}_3 symmetry [23–35]. Introduced with the notation I(2+1)HDM in Ref. [25], the vacuum configuration is chosen that only the scalar doublet even under \mathbb{Z}_3 acquires a vacuum expectation value (vev). The two other doublets, non-invariant under \mathbb{Z}_3 , do not acquire a vev, achieving the vacua alignment $(0, 0, v)$ and an unbroken symmetry. Choosing the fermions to be invariant under \mathbb{Z}_3 , the two inert doublets are part of a stable dark sector. The symmetry being specifically \mathbb{Z}_3

* abreurocha@lip.pt

† rafael.boto@tecnico.ulisboa.pt

‡ miguel.romao@durham.ac.uk

§ pedro.m.figueiredo@tecnico.ulisboa.pt

¶ jorge.romao@tecnico.ulisboa.pt

leads to two mass-degenerate DM states with opposite CP, distinct from a single \mathbb{Z}_2 [36, 37], with only the lightest \mathbb{Z}_2 -odd scalar as the DM candidate, or a $\mathbb{Z}_2 \times \mathbb{Z}_2$ construction [38–40], with two distinct dark sectors, each with one DM scalar candidate. It is then crucial that the scalar potential has a global minimum and it corresponds to the desired $(0, 0, v)$ configuration. We revisit the formulation of the scalar potential leading to the theoretical conditions for consistency.

We perform a comprehensive scan of the \mathbb{Z}_3 3HDM parameter space. Every relevant theoretical, experimental and astrophysical constraint is applied. This includes the recent and stringent direct detection bounds by the LZ collaboration [41] and the collider data on the 125 GeV Higgs boson invisible branching ratio from ATLAS [42]. The validation process includes comparison of the one property of DM that is precisely measured with the numerically calculated prediction, the DM relic density of $\Omega_{\text{DM}} = 0.1200 \pm 0.0012$ [43]. Given the opposing tension in scalar DM models between the measured relic abundance and the non-observation in detection experiments [44], we follow a Machine Learning (ML) approach to perform the constrained sampling of the model.

In the past 10 years, ML has been integrated in many of the different areas of Particle Physics, with modern reviews documenting the constant advancement of applications [45–48]. Our goal is to efficiently obtain solutions that meet a long list of constraints, as a optimization problem. There have been multiple cases of success with different approaches, with their benefits and disadvantages [48–60]. Starting from a model where valid training data is not easily obtainable, we follow a variant of the Evolutionary Strategy algorithm, first introduced in Ref. [61], combined with an histogram based anomaly detection procedure used for Novelty Reward, developed in Ref. [29]. We improve on the previous methodology by considering a novel prototype selection approach, using information of already completed runs to optimally select the starting points for future runs, in regions that are less populated. The technique presented allows the automatized identification of representative benchmark solutions of a chosen subset in parameter and/or observable space. The approach also enables more efficient exploration of the model, yielding a wider range of allowed dark matter masses and expanding upon the existing literature [25].

The work is organized as follows. In Section II, we recapitulate the \mathbb{Z}_3 symmetric scalar potential and discuss the conditions for the boundedness from below and the desired $(0, 0, v)$ vacua to be the global minima. In Section III, we describe the strategy developed for sampling the valid parameter space of the model. In Section IV, we list the constraints included in the ML sampling algorithm. Section V is dedicated to our results, first by setting the mixing angle θ to $\frac{\pi}{4}$, under the assumptions of Ref. [25], followed by a study on possible deviations from this condition. After summarizing our conclusions in Section VI, we present additional details regarding contributions to the relic density in Appendix A and methods to improve our sampling in Appendix B.

II. THE \mathbb{Z}_3 3HDM

A. The Model

We consider a 3HDM with a Lagrangian invariant under a \mathbb{Z}_3 symmetry, satisfying

$$\mathbb{Z}_3 : \phi_1 \rightarrow \omega \phi_1, \quad \phi_2 \rightarrow \omega^2 \phi_2, \quad \phi_3 \rightarrow \phi_3, \quad (1)$$

with $\omega = e^{\frac{2\pi i}{3}}$. With the parametrization used in Refs. [26–29], the resulting potential takes the form

$$\begin{aligned} V = & m_{11}^2(\phi_1^\dagger\phi_1) + m_{22}^2(\phi_2^\dagger\phi_2) + m_{33}^2(\phi_3^\dagger\phi_3) \\ & + \lambda_1(\phi_1^\dagger\phi_1)^2 + \lambda_2(\phi_2^\dagger\phi_2)^2 + \lambda_3(\phi_3^\dagger\phi_3)^2 \\ & + \lambda_4(\phi_1^\dagger\phi_1)(\phi_2^\dagger\phi_2) + \lambda_5(\phi_1^\dagger\phi_1)(\phi_3^\dagger\phi_3) + \lambda_6(\phi_2^\dagger\phi_2)(\phi_3^\dagger\phi_3) \\ & + \lambda_7(\phi_1^\dagger\phi_2)(\phi_2^\dagger\phi_1) + \lambda_8(\phi_1^\dagger\phi_3)(\phi_3^\dagger\phi_1) + \lambda_9(\phi_2^\dagger\phi_3)(\phi_3^\dagger\phi_2) \\ & + \left[\lambda_{10}(\phi_1^\dagger\phi_2)(\phi_1^\dagger\phi_3) + \lambda_{11}(\phi_1^\dagger\phi_2)(\phi_3^\dagger\phi_2) + \lambda_{12}(\phi_1^\dagger\phi_3)(\phi_2^\dagger\phi_3) + \text{h.c.} \right], \end{aligned} \quad (2)$$

having the direct relation to the convention used in Ref. [25] by,

$$\begin{aligned} \lambda_1 & \rightarrow \lambda_{11}, & \lambda_2 & \rightarrow \lambda_{22}, & \lambda_3 & \rightarrow \lambda_{33}, & \lambda_4 & \rightarrow \lambda_{12}, \\ \lambda_5 & \rightarrow \lambda_{13}, & \lambda_6 & \rightarrow \lambda_{23}, & \lambda_7 & \rightarrow \lambda'_{12}, & \lambda_8 & \rightarrow \lambda'_{13}, \\ \lambda_9 & \rightarrow \lambda'_{23}, & \lambda_{10} & \rightarrow \lambda_1, & \lambda_{11} & \rightarrow \lambda_2, & \lambda_{12} & \rightarrow \lambda_3. \end{aligned} \quad (3)$$

Aiming for a scenario with two DM states, we consider the vacuum alignment $\langle\phi_1\rangle = \langle\phi_2\rangle = 0$ and $\langle\phi_3\rangle = v$, thus keeping the \mathbb{Z}_3 symmetry unbroken, defined by the transformation in Eq. (1). After Spontaneous Symmetry Breaking (SSB), the doublets are developed in the symmetry basis as

$$\phi_1 = \begin{pmatrix} H_1^+ \\ \frac{x_1 + iy_1}{\sqrt{2}} \end{pmatrix}, \quad \phi_2 = \begin{pmatrix} H_2^+ \\ \frac{x_2 + iy_2}{\sqrt{2}} \end{pmatrix}, \quad \phi_3 = \begin{pmatrix} G^+ \\ \frac{v + h + iG^0}{\sqrt{2}} \end{pmatrix}. \quad (4)$$

The corresponding minimization condition is given by

$$v^2 = \frac{m_h^2}{2\lambda_3}. \quad (5)$$

The mass matrices of the fields x_i and y_i in the electroweak basis are, for the neutral CP-even scalars,

$$\mathcal{M}_{\text{even}}^2 = \begin{pmatrix} m_{11}^2 + \frac{1}{2}v^2(\lambda_5 + \lambda_8) & \frac{1}{2}v^2\lambda_{12} & 0 \\ \frac{1}{2}v^2\lambda_{12} & m_{22}^2 + \frac{1}{2}v^2(\lambda_6 + \lambda_9) & 0 \\ 0 & 0 & 2\lambda_3v^2 \end{pmatrix} \quad (6)$$

for the CP-odd scalars,

$$\mathcal{M}_{\text{odd}}^2 = \begin{pmatrix} m_{11}^2 + \frac{1}{2}v^2(\lambda_5 + \lambda_8) & -\frac{1}{2}v^2\lambda_{12} & 0 \\ -\frac{1}{2}v^2\lambda_{12} & m_{22}^2 + \frac{1}{2}v^2(\lambda_6 + \lambda_9) & 0 \\ 0 & 0 & 0 \end{pmatrix} \quad (7)$$

and for the charged

$$\mathcal{M}_{\text{charged}}^2 = \begin{pmatrix} m_{11}^2 + \frac{1}{2}v^2\lambda_5 & 0 & 0 \\ 0 & m_{22}^2 + \frac{1}{2}v^2\lambda_6 & 0 \\ 0 & 0 & 0 \end{pmatrix}. \quad (8)$$

which is already diagonal. The masses in the physical basis for the neutral scalars can then be obtained by applying the rotation

$$R\mathcal{M}^2R^T = \text{diag}(m_1^2, m_2^2, m_3^2) \quad (9)$$

with a matrix of the form

$$R_{\theta_i} = \begin{pmatrix} \cos\theta_i & \sin\theta_i & 0 \\ -\sin\theta_i & \cos\theta_i & 0 \\ 0 & 0 & 1 \end{pmatrix}. \quad (10)$$

Here, $\theta_i = (\theta_x, \theta_y)$ for the scalar fields x_i and the pseudoscalar fields y_i , respectively, with $-\pi/2 < \theta_i \leq \pi/2$. The diagonalization yields that $\tan(2\theta_x) = -\tan(2\theta_y)$, resulting in a simpler transformation that depends only on a single angle θ , of the form

$$\begin{pmatrix} H_1 \\ H_2 \end{pmatrix} = \begin{pmatrix} c_\theta & s_\theta \\ -s_\theta & c_\theta \end{pmatrix} \begin{pmatrix} x_1 \\ x_2 \end{pmatrix}, \quad \begin{pmatrix} A_1 \\ A_2 \end{pmatrix} = \begin{pmatrix} c_\theta & -s_\theta \\ s_\theta & c_\theta \end{pmatrix} \begin{pmatrix} y_1 \\ y_2 \end{pmatrix}, \quad (11)$$

with $c_\theta = \cos(\theta)$ and $s_\theta = \sin(\theta)$. The charged-scalar fields require no further transformations as they are already in the physical basis. The resulting expressions for the masses are then,

$$\begin{aligned}
m_{H_1}^2 &= m_{A_1}^2 = \left(m_{11}^2 + \frac{1}{2}v^2(\lambda_5 + \lambda_8) \right) c_\theta^2 + \left(m_{22}^2 + \frac{1}{2}v^2(\lambda_6 + \lambda_9) \right) s_\theta^2 + \lambda_{12}v^2 s_\theta c_\theta, \\
m_{H_2}^2 &= m_{A_2}^2 = \left(m_{22}^2 + \frac{1}{2}v^2(\lambda_6 + \lambda_9) \right) c_\theta^2 + \left(m_{11}^2 + \frac{1}{2}v^2(\lambda_5 + \lambda_8) \right) s_\theta^2 - \lambda_{12}v^2 s_\theta c_\theta, \\
m_{H_1^\pm}^2 &= m_{11}^2 + \frac{\lambda_5 v^2}{2}, \\
m_{H_2^\pm}^2 &= m_{22}^2 + \frac{\lambda_6 v^2}{2}.
\end{aligned} \tag{12}$$

Following Ref. [25], we take as independent parameters

$$m_{H_1}, m_{H_2}, m_{H_1^\pm}, m_{H_2^\pm}, \theta, g_1, g_2, \lambda_1, \lambda_4, \lambda_7, \lambda_{10}, \lambda_{11}, \tag{13}$$

where θ is the mixing angle between ϕ_1 and ϕ_2 , $g_1 = g_{hH_1H_1}/v$ is the couplings between H_1 and the 125 GeV Higgs and $g_2 = g_{hH_1H_2}/v$. In this work, the signs of g_1 and g_2 are defined by the Feynman rules and are symmetric of the ones in Ref. [25]. We know the mass of the h_{125} and the vev to be

$$v = \left(\sqrt{2}G_F \right)^{-1/2} \approx 246 \text{ GeV}, \quad m_h = 125 \text{ GeV}, \tag{14}$$

from which we can get m_{33}^2 and λ_3 with the stationarity conditions in Eq. (5). The other parameters of the potential can be obtained from the above. We detect a mismatch between the expressions of Ref. [25] and the ones we derived, coinciding only for $\theta = \frac{\pi}{4}$,

$$\begin{aligned}
\lambda_3 &= \frac{m_h^2}{2v^2}, \\
\lambda_5 &= -g_1 + \frac{2m_{H_1^\pm}^2}{v^2} - \frac{2m_{H_1^0}^2}{v^2} + g_2 \tan(\theta), \\
\lambda_6 &= -g_1 + \frac{2m_{H_2^\pm}^2}{v^2} - \frac{2m_{H_1^0}^2}{v^2} - g_2 \cot(\theta), \\
\lambda_8 &= \frac{1}{v^2} \left(-2m_{H_1^\pm}^2 + m_{H_1^0}^2 + m_{H_2^0}^2 + (m_{H_1^0}^2 - m_{H_2^0}^2) \cos(2\theta) \right), \\
\lambda_9 &= \frac{1}{v^2} \left(-2m_{H_2^\pm}^2 + m_{H_1^0}^2 + m_{H_2^0}^2 + (-m_{H_1^0}^2 + m_{H_2^0}^2) \cos(2\theta) \right), \\
\lambda_{12} &= \frac{1}{v^2} \left((m_{H_1^0}^2 - m_{H_2^0}^2) \sin(2\theta) \right), \\
m_{11}^2 &= m_{H_1^0}^2 + \frac{1}{2}v^2 \left(g_1 - g_2 \tan(\theta) \right), \\
m_{22}^2 &= m_{H_2^0}^2 + \frac{1}{2}v^2 \left(g_1 + g_2 \cot(\theta) \right), \\
m_{33}^2 &= -\lambda_3 v^2.
\end{aligned} \tag{15}$$

As the squared masses are all positive, we may conclude that we are at the local minimum. Moreover, we obtain the mass degeneracy conditions $m_{H_1} = m_{A_1}$ and $m_{H_2} = m_{A_2}$. This relation is not arbitrary, as it arises directly from the symmetry and the vacuum configuration.

Regarding the interactions with fermions and gauge bosons, all SM fields are chosen to be even under \mathbb{Z}_3 . Therefore, all fermion fields couple only with ϕ_3 and the Yukawa couplings follow as identical to the SM. This realises a Type-I model which has no FCNCs at tree-level.

B. Bounded from below conditions

As a consistency requirement for any physical theory, the scalar potential must satisfy conditions that ensure it possesses a stable minimum. The potential given in Eq. (2) must be bounded from below, meaning that there is no direction in field space along which the value of the potential tends to minus infinity. Such directions can be classified into neutral directions, which do not break electric charge, or charge-breaking (CB) directions. Ref. [62] has shown, for the specific case of the $U(1) \times U(1)$ symmetric 3HDM, that the potential can be unbounded from below along CB directions despite satisfying the conditions along neutral directions.

Following the procedure in Ref. [63], the quartic part of the potential can be rewritten into a piece invariant under rephasings, similar for all symmetry constrained 3HDM potentials, with terms related to neutral (V_N) and CB (V_{CB}) directions, and the \mathbb{Z}_3 -specific terms as

$$V_{\text{quartic}} = V_N + V_{CB} + V_{\mathbb{Z}_3}, \quad (16)$$

where

$$V_N = \lambda_1(\phi_1^\dagger\phi_1)^2 + \lambda_2(\phi_2^\dagger\phi_2)^2 + \lambda_3(\phi_3^\dagger\phi_3)^2 \\ + (\lambda_4 + \lambda_7)(\phi_1^\dagger\phi_1)(\phi_2^\dagger\phi_2) + (\lambda_5 + \lambda_8)(\phi_1^\dagger\phi_1)(\phi_3^\dagger\phi_3) + (\lambda_6 + \lambda_9)(\phi_2^\dagger\phi_2)(\phi_3^\dagger\phi_3), \quad (17)$$

$$V_{CB} = -\lambda_7 z_{12} - \lambda_8 z_{13} - \lambda_9 z_{23}, \quad (18)$$

$$V_{\mathbb{Z}_3} = \lambda_{10}(\phi_1^\dagger\phi_2)(\phi_1^\dagger\phi_3) + \lambda_{11}(\phi_1^\dagger\phi_2)(\phi_3^\dagger\phi_2) + \lambda_{12}(\phi_1^\dagger\phi_3)(\phi_2^\dagger\phi_3) + \text{h.c.}, \quad (19)$$

with the definition [62]

$$z_{ij} = (\phi_i^\dagger\phi_i)(\phi_j^\dagger\phi_j) - (\phi_i^\dagger\phi_j)(\phi_j^\dagger\phi_i) \quad (\text{no sum}). \quad (20)$$

The vevs of the doublets are parametrized as

$$\phi_1 = \sqrt{r_1} \begin{pmatrix} \sin(\alpha_1) \\ \cos(\alpha_1)e^{i\beta_1} \end{pmatrix}, \quad \phi_2 = \sqrt{r_2}e^{i\gamma} \begin{pmatrix} \sin(\alpha_2) \\ \cos(\alpha_2)e^{i\beta_2} \end{pmatrix}, \quad \phi_3 = \sqrt{r_3} \begin{pmatrix} 0 \\ 1 \end{pmatrix}, \quad (21)$$

allowing V_N to be written in the form

$$V_N = \frac{1}{2} \sum_{ij} r_i A_{ij} r_j, \quad \text{with} \quad (A)_{ij} = \begin{pmatrix} 2\lambda_1 & \lambda_4 + \lambda_7 & \lambda_5 + \lambda_8 \\ \lambda_4 + \lambda_7 & 2\lambda_2 & \lambda_6 + \lambda_9 \\ \lambda_5 + \lambda_8 & \lambda_6 + \lambda_9 & 2\lambda_3 \end{pmatrix}, \quad (22)$$

which, following Klimenko [64] and Kannike [65], allows the formulation of the neutral copositivity conditions that assure this part of the potential is BFB, by the quadratic form A being positive definite for $r_i \geq 0$. The full \mathbb{Z}_3 symmetric potential, however, has no known necessary and sufficient conditions, so we follow the method similar to Ref. [63] to, at least, obtain sufficient conditions by bounding the potential with a lower one that can be reduced to a quadratic form, as in Eq. (22). The CB part can be simplified to

$$V_{CB} \geq V_{CB}^{\text{lower}} = r_1 r_2 \min(0, -\lambda_7) + r_1 r_3 \min(0, -\lambda_8) + r_2 r_3 \min(0, -\lambda_9), \quad (23)$$

and the \mathbb{Z}_3 -specific part yields

$$V_{\mathbb{Z}_3} \geq V_{\mathbb{Z}_3}^{\text{lower}} = -2(|\lambda_{10}| + |\lambda_{11}|)r_1 r_2 - 2(|\lambda_{10}| + |\lambda_{12}|)r_1 r_3 - 2(|\lambda_{11}| + |\lambda_{12}|)r_2 r_3. \quad (24)$$

Finally, the sufficient conditions for the \mathbb{Z}_3 potential to be BFB consist of the requirement that the quadratic form, A in Eq. (22), is positive definite with the following entries A_{ij} [29, 66],

$$A_{11} = 2\lambda_1, \\ A_{12} = \lambda_4 + \lambda_7 + \min(0, -\lambda_7) - 2|\lambda_{10}| - 2|\lambda_{11}|, \\ A_{13} = \lambda_5 + \lambda_8 + \min(0, -\lambda_8) - 2|\lambda_{10}| - 2|\lambda_{12}|, \\ A_{22} = 2\lambda_2, \\ A_{23} = \lambda_6 + \lambda_9 + \min(0, -\lambda_9) - 2|\lambda_{11}| - 2|\lambda_{12}|, \\ A_{33} = 2\lambda_3. \quad (25)$$

C. Global Minimum

Besides imposing the potential be BFB, we must guarantee the minimum we want to study is also the global minimum of the potential. We are interested in the 2-Inert minimum given by the vacuum structure $(0, 0, v)$, as it allows for a multi-component DM scenario. To check if we are at the global minimum, a routine was implemented in the minimization program `Minuit` [67] by CERN. With this procedure, after imposing the BFB conditions, we found two other competing minima, $(v, 0, 0)$ and $(0, v, 0)$. These can be written in terms of the potential parameters on that point as

$$\text{The case } v_1 = v, v_2 = 0, v_3 = 0 : \quad V_{(v,0,0)}^{\min} = -\frac{m_{11}^4}{4\lambda_1}, \quad (26)$$

$$\text{The case } v_1 = 0, v_2 = v, v_3 = 0 : \quad V_{(0,v,0)}^{\min} = -\frac{m_{22}^4}{4\lambda_2}, \quad (27)$$

$$\text{The 2-Inert vacua } v_1 = v_2 = 0, v_3 = v : \quad V_{(0,0,v)}^{\min} = -\frac{m_{33}^4}{4\lambda_3}. \quad (28)$$

Given these conditions, for a given point, we may compare the value of the potential with these two cases and discard the point if either of the minima falls below the desired 2-Inert case in Eq. (28). Then, as a sanity check, we confirm numerically that indeed no lower-lying minimum is found.

III. MACHINE LEARNING SCAN STRATEGY

We allow values for the parameters of Eq. (13) in the ranges

$$\begin{aligned} \lambda_1, \lambda_4, \lambda_7, \lambda_{10}, \lambda_{11} &\in \pm [10^{-3}, 10] ; \\ m_{H_1} = m_{A_1}, m_{H_2} = m_{A_2} &\in [50, 1000] \text{ GeV} ; \\ m_{H_1^\pm}, m_{H_2^\pm} &\in [70, 1000] \text{ GeV} ; \\ g_1, g_2 &\in [-0.5, 0.5] ; \quad \theta \in \left[-\frac{\pi}{2}, \frac{\pi}{2} \right] ; \end{aligned} \quad (29)$$

and impose the condition, without loss of generality, that $m_{H_1} < m_{H_2}$. The lower limit on the mass of the charged scalars follows from Ref. [68]. Although this bound has not been established within the context of the current model, we take it as a conservative lower bound on the masses of all charged scalars.

After rotating the DM fields to the mass basis, there are two distinct sectors: the dark- \mathbb{Z}_3 sector, constituted by the fields in ϕ_1 and ϕ_2 , and the active or SM sector, constituted by the fields in ϕ_3 and all SM fermions. This differs from the two-component DM case, also with two additional inert doublet scalars of Ref. [40], as it has three distinct sectors. Connections among different sectors can only occur due to gauge bosons or the interactions in the scalar potential.

A. Evolutionary Strategy and Novelty Detection for Parameter Space Exploration

We employ the ML-based scan strategy first described in Ref. [61]. The astrophysical data from relic density, direct and indirect detection are considered in the optimisation procedure, taking advantage of its rapid convergence and capacity to explore the viable parameter space of a given model, as further demonstrated in Refs. [29, 69–73]. The observables are calculated within a black-box, a combination of an in-house code and calls to public software, `HiggsTools` [74] and `micrOmegas` [75], which are then introduced into the ML pipeline. Then, they are checked with a constraint function, C , defined as

$$C(\mathcal{O}) = \max(0, -\mathcal{O} + \mathcal{O}_{LB}, \mathcal{O} - \mathcal{O}_{UB}), \quad (30)$$

where \mathcal{O} is the value of an observable or a constrained quantity, \mathcal{O}_{LB} is its lower bound, and \mathcal{O}_{UB} its upper bound. The constraint function $C(\mathcal{O})$ returns 0 if and only if \mathcal{O} lies within the specified interval. Otherwise, it returns a positive number quantifying *how far* the value of the observable lies from the specified bounds. Finding points that

satisfy a given constraint is equivalent to minimizing the respective $C(\mathcal{O})$ function. To account for multiple observables and parameter bounds simultaneously, one sums all the constraints $C(\mathcal{O})$ into a single loss function, L ,¹ as

$$L(\hat{\theta}) = \sum_{i=1}^{N_c} C(\mathcal{O}_i(\hat{\theta})), \quad (31)$$

where $\hat{\theta}$ is the input vector in the parameter space and N_c is the number of constraints considered. The sampling algorithm chosen to optimize the loss function in Eq. (31) is the Covariant Matrix Adaptation Evolutionary Strategy optimiser (CMA-ES) [76–79], later augmented with a novelty reward mechanism based on density estimation, using an Histogram Based Outlier Score (HBOS) [80, 81] in Ref. [29]. This procedure enhances exploration in some chosen parameters and/or observables of interest by adding a penalty p to the loss function L . The penalties are normalized to $p \in [0, 1]$, such that new points receive a penalty of value 0, corresponding to a lower density, while points similar to previously explored ones receive penalties approaching maximum value of 1. This adjustment encourages CMA-ES to explore novel regions by penalising the loss function when constraints are satisfied and solutions are near already discovered areas. Throughout the analysis of the model in Section V, we specify which parameters are receiving *focus*, meaning that exploration in the plane of those quantities is actively being penalised and benefiting from the novelty reward features.

B. Prototype Selection for Seed Acquisition

Due to the exploitative and local search nature of CMA-ES, several independent runs of the algorithm are necessary to fully paint a picture of the global valid parameter space. This typically leads to convergence to a few disconnected regions, after some initial runs. The density of points in each of those regions is a good indicative of the easiness of convergence the algorithm has towards that particular region. This happens due to the shape of the constrained parameter space hypersurface that CMA-ES is learning. Being so, it is likely that a considerable portion of future runs will converge to similar previously discovered regions, thus hindering exploration. In order to obtain a global picture of the valid parameter space, one can force exploration by using seeds where new runs are to be initialised. These seeds can be selected amongst previously obtained points from sparsely populated regions, thus forcing CMA-ES, aided by the novelty reward mechanism, to effectively expand these regions.

The process of seed selection can be manually carried out by the user after careful data analysis to identify potential regions of interest for further exploration. Although this method can be valuable for seed selection immediately after initial runs, it can quickly turn into a time consuming and cumbersome process after a considerable amount of valid points has been amassed.

In this work we develop three promising methods for seed selection based on known ML algorithms: Histogram Gradient Boosting Classifier (HGBC) [82], Mini-Batch k -Means (MBKM) [83], and Local Outlier Factor (LOF) [84]. The prototype selection criteria for seeds is partially automated, while still allowing user intervention to customize acceptance quantiles, cluster selection, and other parameters. Further details on the implementation and how to employ such techniques can be found in Appendix B. The three approaches are distinct and thus lead to different seed choices. This approach shares similarities with active learning, shown to have success in similar applications [54].

HGBC can be used to select seeds from globally underdense regions. After the addition of a mask of uniform noise over the data, we can train HGBC to distinguish the real data from the added noise. We can select the most outlying quantile in the collected valid points, typically 1% or less, to be used as seeds. This way, we are selecting the points which are harder to distinguish from uniform noise, corresponding to the ones in less densely populated regions, in need for further exploration.

MBKM can be used to select seeds from the edges of clustered regions. Once trained on the dataset of valid points, we can select the points from each cluster that are farthest away from the respective centroid. This way, we are sampling seeds that lie on the frontier of each cluster. These seeds can then be used for future runs to effectively expand the frontiers of those clustered regions. k -Means has been previously successfully used for prototype selection for Quantum ML collider analysis [85].

Lastly, we can use LOF to select seeds from the fringes of local neighbourhoods in the dataset of valid points. After training, LOF can give an anomaly score for each data point corresponding to its local density deviation with respect

¹ For a multi-objective alternative approach see Ref. [69].

to its local neighbours. Like in the HGBC case, we can select a quantile ($< 1\%$) for the highest anomaly scores in the data.

Moreover, there are regions which seem easy to explore when projected on a 2D plane, yet may be completely disconnected on the hypersurface supporting the valid points, given its non-convex and multi-dimensional nature. This creates dense shapes, with close neighbouring regions completely empty, as explicitly shown in Appendix B where we further detail the new methodologies listed herein. As these areas are very populated, it becomes harder for HGBC to select points there without increasing the acceptance too much and end up with a sparse set of seeds, useless to focus on specific areas. To address this, one can use LOF to efficiently target the regions of interest as it can easily detect local density deviations and target the points that lie in the fringes of these areas. Alternatively, one can train MBKM, select the clusters of interest, isolate the points that lie furthest from its centroids and use them for seeds. This combined with a constraint that enforces exploration on a subset of the parameter space greatly improves the convergence rate.

IV. CONSTRAINTS

For the single-objective optimization algorithm, we consider a loss function that sums all the different constraints in the form of $C(\mathcal{O})$ functions, defined in Eq. (30) for a chosen lower and upper bound. The constraint set incorporates theoretical bounds, experimental measurements, and selection cuts on an equal basis within the unified objective function.² For the theoretical bounds, we apply the constraints from BFB and global minimum described in Section II. Perturbative unitarity is considered following Refs. [86, 87] and compliance with the oblique parameters STU from the global electroweak fit [88], calculating the numerical predictions using the formulae in Ref. [89].

As a Type-I model, all Yukawa fermion-Higgs couplings are identical to the SM. With the charged scalars also inert, the model bypasses all flavour constraints, such as bounds on masses from $B \rightarrow X_s \gamma$.

A. Collider constraints

We calculate all processes at lowest non-trivial order and take all input parameters at the electroweak scale. Our in-house program includes the latest LHC bounds on the h_{125} signal strengths with the full Run 2 data collected at 13 TeV, for the different production and decay modes, following the ATLAS results in fig. 3 of Ref. [90]. We require agreement with the discovered Higgs boson signal strengths at 2σ . For a given production and decay channel, the Higgs signal strength is defined as

$$\mu_i^f = \frac{\sigma_i^{\text{3HDM}}(pp \rightarrow h_{125})}{\sigma_i^{\text{SM}}(pp \rightarrow h_{125})} \times \frac{\text{BR}^{\text{3HDM}}(h_{125} \rightarrow f)}{\text{BR}^{\text{SM}}(h_{125} \rightarrow f)}, \quad (32)$$

The upper limit on the Higgs total decay width is set by Ref. [91] at $\Gamma_{\text{tot}} \leq 7.5 \text{ MeV}$ and we forbid decays of SM gauge bosons into the new scalars, imposing [38],

$$m_{H_i} + m_{H_i^\pm} \geq m_W^\pm, \quad m_{A_i} + m_{H_i^\pm} \geq m_W^\pm, \quad m_{H_i} + m_{A_i} \geq m_Z, \quad 2m_{H_i^\pm} \geq m_Z. \quad (33)$$

In order to evade the bounds from long-lived charged particle searches given in Ref. [92], we set the upper limit on the charged scalar lifetime of $\tau \leq 10^{-7} \text{ s}$.

If the DM mass $m_{\text{DM}} \lesssim m_{h_{125}}/2$, the Higgs boson can decay invisibly. This decay contributes to the Higgs total width and modifies its branching ratios. The invisible branching ratio at 95% C.L. is given by

$$\text{BR}(h_{125} \rightarrow \text{invisible}) = \frac{\Gamma(h_{125} \rightarrow \chi\chi)}{\Gamma_{h_{125}}^{\text{SM}} + \Gamma(h_{125} \rightarrow \chi\chi)} \leq 0.107 \pm 0.077 \quad (95\% \text{ CL}), \quad (34)$$

from a combined ATLAS analysis [42], where $\Gamma(h_{125} \rightarrow \chi\chi)$ is the partial width of the Higgs into a pair of DM particles and the denominator is the total width of the Higgs boson in the given model.

² There is however a possibility of imposing a hierarchical sequence [69, 70], especially important in scenarios where physical masses are derived quantities that must be positive. In this study we are not in this situation.

The points are also passed through `HiggsTools-1.1.3` [74], imposing current bounds from searches for additional scalars with the most recent module `HiggsBounds (HB)`, version 1.6 of the dataset. We also require a 3σ agreement with the $\Delta\chi^2$ test from the `HiggsSignals` module of `HiggsTools-1.1.3`. We later verified agreement with the new release of `HiggsTools-1.2` and the `HiggsBounds dataset-1.7`.

B. Dark Matter Constraints

We implement the model in `FeynMaster-2.1` [93–95], combining the public codes `FeynRules-2.3.49` [96, 97], `QGRAF 4.0.5` [98] and `FeynCalc-10.1.0` [99–101], that can then export the files necessary to run `micrOmegas-6.2.3` [75]. The relic density, scattering amplitudes, and annihilation cross sections are then computed using the `DarkOmegaN` routine in the public code `micrOmegas-6.2.3` [75].

1. Relic Density

The total DM relic density is given by the sum of the individual contributions from each DM component. We impose consistency with the measurement reported by the *Planck* Collaboration [43] up to 3σ ,

$$\Omega_T h^2 = \Omega_1 h^2 + \Omega_2 h^2 \stackrel{Planck}{=} 0.1200 \pm 0.0012. \quad (35)$$

In order to achieve the correct results for the relic calculation in this model, one has to employ the appropriate routine of `micrOMEGAS-6.2.3`, `DarkOmegaN`, as for higher temperatures, co-scattering of the form $\chi_i \text{ SM} \rightarrow \chi_i' \text{ SM}'$ and DM conversion processes are essential to maintain chemical equilibrium. A detailed discussion can be found in Appendix A. Furthermore, as both DM components, H_1 and A_1 , arise from the same doublet, they share the same couplings, resulting in an equal contribution from both components to the relic. The contribution from H_2 and A_2 is negligible, as they are heavier and decay completely.

2. Direct Detection

The direct detection experiments look for the interaction of the DM particles with regular matter, through measuring the recoil energy of nuclei. The most recent constraints from DM-nucleon scattering are provided by LZ 2025 [41], shown in Fig. 1 along with the XLZD predictions [102] and the lines for the neutrino fog region³ [103].

To compare the calculated predictions with these limits, we follow the procedure described in Ref. [104], computing the spin-independent (SI) DM-nucleus cross section for a Xenon target,

$$\sigma_{\text{SI}}^{\text{Xe},k} = \frac{4\mu_k^2 [Zf_p + (A-Z)f_n]^2}{\pi A^2}, \quad (36)$$

where μ_k is the reduced mass of the k -th DM component, and f_p (f_n) denote the effective couplings to protons (neutrons). Since the dark sector comprises two DM components, we rescale the scattering cross section of each component according to its relative abundance,

$$\sigma_{\text{SI}}^{\text{r},k} = \sigma_{\text{SI}}^{\text{Xe},k} \xi_k, \quad \xi_k = \frac{\Omega_k}{\Omega_T}. \quad (37)$$

3. Indirect Detection

Indirect detection consists of experimental bounds from the (non-)observation of annihilation or decay products of WIMPs in the Universe. The current limits from the Fermi-LAT satellite on photon fluxes from DM annihilation [108] constrain $\langle\sigma v\rangle$ to be approximately $3 \times 10^{-26} \text{ cm}^3/\text{s}$ for light DM and up to $\sim 10^{-25} \text{ cm}^3/\text{s}$ for heavier DM.

³ The direct detection data files and general layout for all the related plots follows from the public repository by Ciaran O’Hare, available in <https://github.com/cajohare/DirectDetectionPlots>.

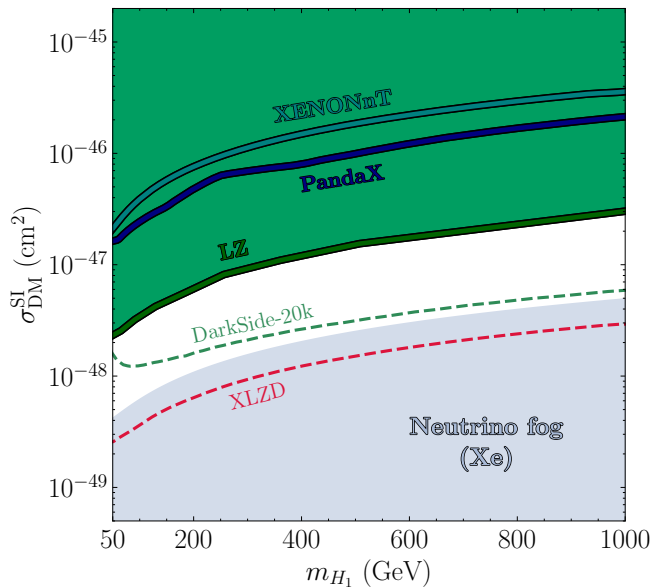


Figure 1: In solid lines, the most recent direct detection limits from XENONnT [105], PandaX-4T [106] and LZ [41] for the mass region of interest. In dashed lines, the projections for the upcoming DarkSide-20k [107] and XLZD [102] experiments, which is expected to breach the neutrino fog in the region of interest for the WIMP mass [103], shown as the grey shaded region.

Following Ref. [109], we find that the most relevant channels within the Fermi-LAT sensitivity region correspond to annihilations into $b\bar{b}$ and electroweak gauge bosons. We therefore require $\langle\sigma v\rangle_{b\bar{b}}$ and $\langle\sigma v\rangle_{VV}$ to satisfy the 95% C.L. Fermi-LAT bounds [108]. Searches for antiprotons with AMS-02 [110, 111] provide even more stringent constraints on WIMP DM. In this case, we again use $\langle\sigma v\rangle_{b\bar{b}}$ and $\langle\sigma v\rangle_{VV}$, and apply the bounds from Ref. [112]. Finally, we note that the H.E.S.S. telescope [113], which observes gamma rays from the Galactic Center, sets the strongest constraints for DM masses above approximately 700 GeV. All these limits and their corresponding exclusion zones are displayed in Fig. 2.

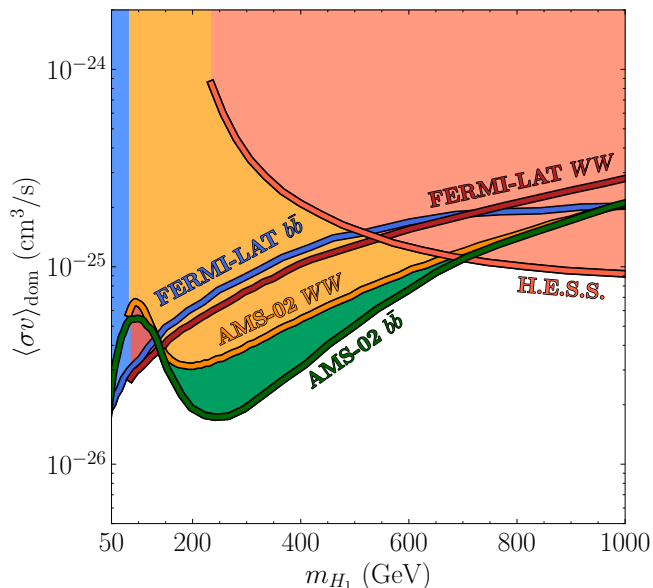


Figure 2: Indirect detection constraints for WW and $b\bar{b}$ channels in the region of interest for the WIMP mass. The experimental lines originate from Fermi-LAT [108], H.E.S.S. [113] and AMS-02 [110, 111], following the approach in Ref. [112].

To account for indirect detection limits, we follow the strategy of Ref. [109] and use our micrOMEGAs-6.2.3 model

implementation to compute the thermally averaged annihilation cross section times velocity, $\langle\sigma v\rangle$. We performed an initial grid-search over the DM mass-relic plane, enforcing its compliance with Planck bounds on the relic density, and selected the dominant annihilation channels for each point. Due to the nature of experimental limits, we sum the contributions from annihilation into WW and ZZ as the same $\langle\sigma v\rangle_{VV}$ signal, while other channels, such as $b\bar{b}$ are considered separately.

Including the indirect constraint function $C(\theta)$ in the ML pipeline results in a significant increase in the time per generation, of order of five times, due to the long calculations of the annihilation and propagation of particles. We omit this constraint from the primary pipeline and instead treat it as an additional validation step after sampling. We follow this choice because we found, similarly to Ref. [40], that for points already consistent with the relic abundance measurement, the current indirect detection bounds result in only mild exclusions.

V. RESULTS

Previous studies on the \mathbb{Z}_3 3HDM as a multi-component DM model have presented an analysis on the limit of $\theta = \frac{\pi}{4}$, as the condition guarantees the vertex $ZH_i A_i \sim \cos(2\theta)$ vanishes [25]. In this limit, the expressions derived for the model parameters coincide with ours and we are able to study the benchmark scenarios proposed. We start by reproducing the results obtained in Ref. [25] and point out the importance of applying the complete BFB conditions for the scalar potential, divided into the neutral, CB and \mathbb{Z}_3 -specific parts.

We then continue in the limit $\theta = \frac{\pi}{4}$ without fixing the benchmark choices for the particle masses, taking into account all the necessary theoretical, collider and astrophysical constraints. Finally, we consider the model without fixing the value for θ .

A. The $\theta = \frac{\pi}{4}$ stability alignment

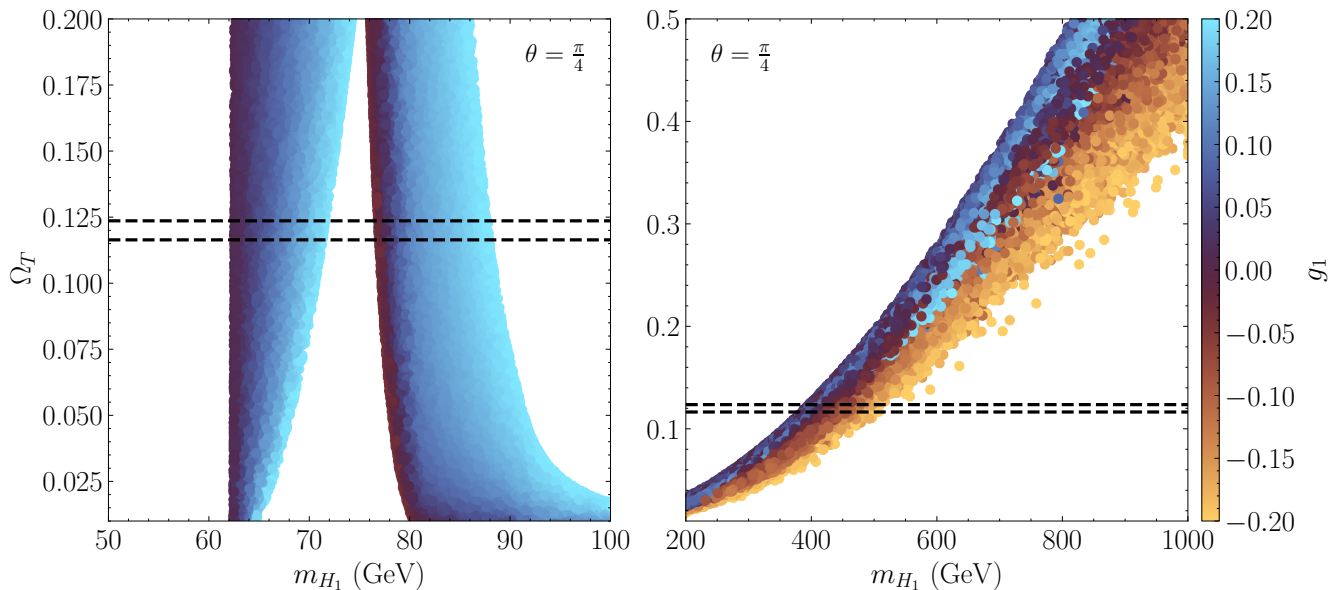


Figure 3: Benchmarks B and G from Ref. [25], for the low and high mass regions, respectively, with colour code for g_1 . All the theoretical constraints are applied, except the CB and \mathbb{Z}_3 -specific BFB conditions described in Eq. (25). `HiggsTools`, direct and indirect detection limits are also not enforced. The horizontal dashed lines are the bounds from relic density.

Following Ref. [25], benchmark scenario B consists of points in the low mass region, $45 \leq m_{\text{DM}} \leq 90$ GeV and benchmark G is the only scenario shown for the high mass region $400 \leq m_{\text{DM}} \leq 900$ GeV. As described in Tab. II of Ref. [25], both benchmarks fix a total of 8 quantities: 5 potential parameters to order $\mathcal{O}(0.1)$ and 3 relations of mass differences, while freely varying λ_{11} ($\lambda_{11} \rightarrow \lambda_2$) and the couplings, g_1 and g_2 . Taking as definitions for the mass difference variables the following relations,

$$\Delta_n = m_{H_2} - m_{H_1}, \quad \Delta_c = m_{H_1^\pm} - m_{H_1}, \quad \delta_c = m_{H_2^\pm} - m_{H_1^\pm}. \quad (38)$$

With the introduced notation, benchmark B corresponds to fixing the variables,

$$\Delta_n = 50 \text{ GeV}, \quad \Delta_c = 60 \text{ GeV}, \quad \delta_c = 10 \text{ GeV}, \quad (39)$$

given that

$$m_{H_1} = m_{A_1} \ll m_{A_2} = m_{H_2} \ll m_{H_1^\pm} \sim m_{H_2^\pm}. \quad (40)$$

Besides the mass-degenerate DM H_1 and A_1 , all other inert particles are much heavier, not allowing co-annihilation with them. As the vertex ZH_iA_i does not exist for the $\theta = \frac{\pi}{4}$ condition, there is also no co-annihilation between H_1 and A_1 . Finally, channels such as hH_1A_1 are also forbidden as the model is CP-conserving. The only co-annihilation processes available are the ones that involve the coupling g_1 , with the H_1H_1h and A_1A_1h vertices.

Benchmark G corresponds to fixing the variables as,

$$\Delta_n = 2 \text{ GeV}, \quad \Delta_c = 0.8 \text{ GeV}, \quad \delta_c = 0.5 \text{ GeV}, \quad (41)$$

with similar values between all neutral and between the charged scalars,

$$m_{H_1} = m_{A_1} \sim m_{A_2} = m_{H_2} \sim m_{H_1^\pm} \sim m_{H_2^\pm}. \quad (42)$$

In this scenario, new channels open up for DM co-annihilation through h and Z mediated processes.

The plots of Fig. 3 show the results of our scans for the two benchmarks scenarios B and G, with a colour code for the value of g_1 . The constraints included are the neutral BFB conditions, STU, global minimum, unitarity, signal strengths, the refactored limits on DM searches, the DM lifetimes, the invisible decay and width of the SM-like Higgs. No agreement with DM direct detection, indirect detection or Higgs data with `HiggsTools` is imposed. In these conditions, we are able to reproduce the behaviour of Figures 1 and 4 of Ref. [25], with the exception of the points in the region below the $m_{\text{DM}} \lesssim m_h/2$ GeV, which we did not find in these scans given the latest bounds of LHC constraints on the invisible branching ratio of the Higgs. The benchmarks B are however found to be excluded when adding the required CB and \mathbb{Z}_3 -specific BFB conditions.

Following Fig. 3-right, the benchmark scenario G allows for valid points in the region $420 \leq m_{\text{DM}} \leq 480$ GeV, comparing with Figure 3 of Ref. [25]. We see the same trend for favoured values of the coupling g_1 , which, again, are symmetric in our study. This range can be expanded to $m_{\text{DM}} \lesssim 700$ GeV when also considering Figure 6 of Ref. [25].

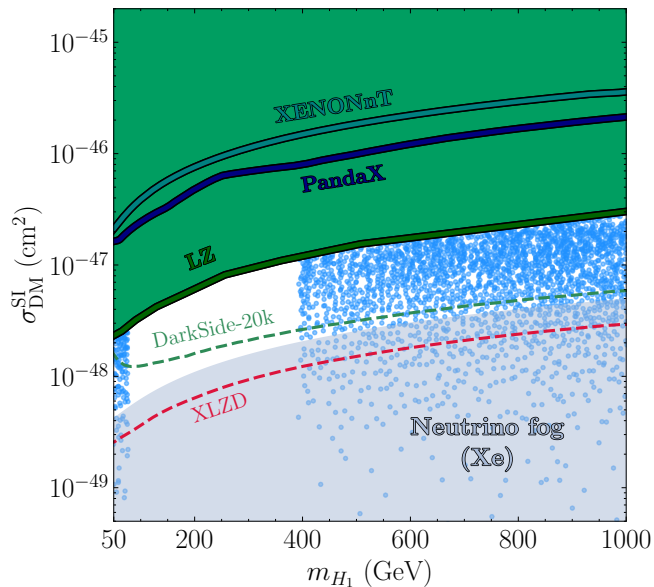


Figure 4: Plane of the direct detection cross-section $\sigma_{H_1}^{SI}$ and m_{DM} . The points in blue pass relic bounds exactly, all theoretical and experimental constraints. The lines shown are the experimental upper bounds from XENONnT [105], PandaX-4T [106] and LZ [41]. In dashed lines, the projections for the next generation experiments DarkSide-20k [107] and XLZD [102] experiments. The neutrino fog [103] is shown as the grey shaded region.

After imposing all the required BFB conditions, we now scan the full mass range in the same limit $\theta = \frac{\pi}{4}$, with a vanishing $ZH_i A_i \sim \cos(2\theta)$ vertex. In Fig. 4, we show the results of scans together with the direct detection experimental limits from LZ in blue [41], the prospects of XLZD in red [102, 114] and the neutrino fog in grey, along with the older experimental limits. These points are in full agreement with the relic density bounds and HiggsTools [74]. In these plots, we see how it is possible to populate the high mass range of the model, which was not covered in Ref. [25]. The coupling g_1 is extremely constrained by the current bounds, yet it is not excluded by future experiments with points inside the neutrino fog region, as described in Refs. [103, 115, 116].

In order to improve the coverage of the parameter space, we follow the strategy of extracting *seeds* from the points in Fig. 4 to be used for subsequent runs. Combining this with *novelty reward* on the parameters and observables of interest, such as m_{DM} , g_1 and Ω_T , we can explore these planes efficiently. Shown in Fig. 5, we observe that it is possible to cover the entire high mass region above $m_{\text{DM}} \gtrsim 380$ GeV while satisfying every constraint.

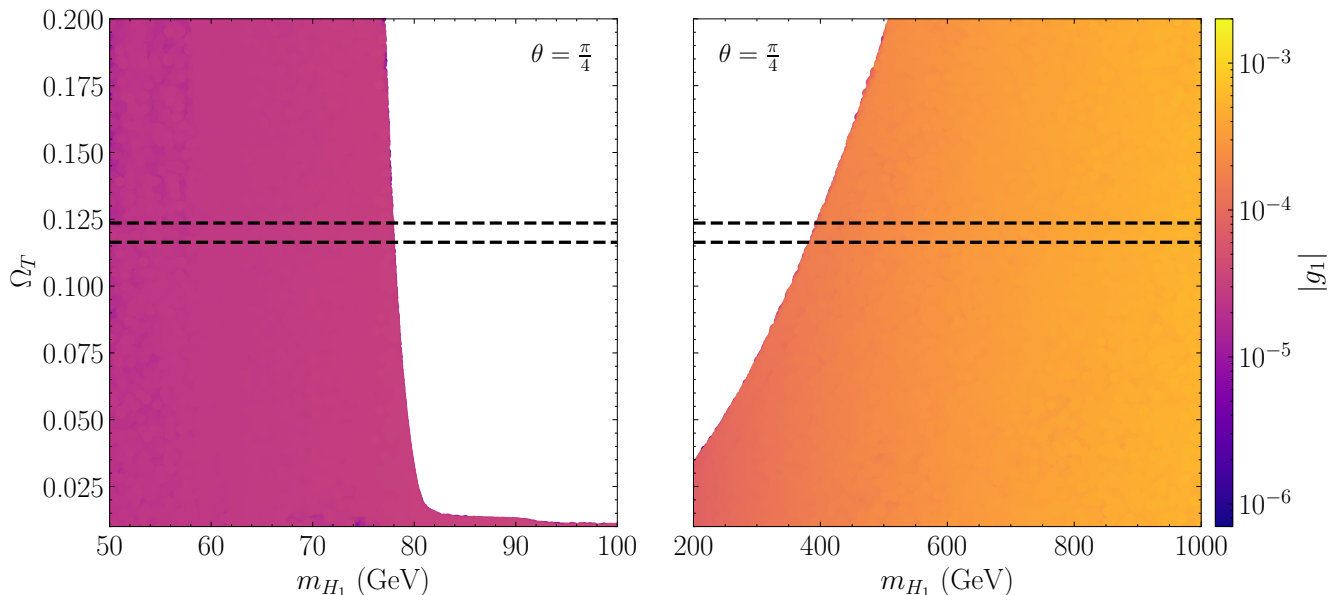


Figure 5: Results obtained for the limit $\theta = \frac{\pi}{4}$ without fixing any of the variables in Eq. (38), with colour code for $|g_1|$. All necessary theoretical constraints are applied, along with the relevant updated bounds from HiggsTools and direct detection. These points are sampled using *seeds* and *focus* on the parameters and observables of interest shown.

We point out that the current indirect detection constraints pose only mild exclusions for this model, similar to the $\mathbb{Z}_2 \times \mathbb{Z}'_2$ 3HDM of Ref. [40], and the dominant channel is also $H_1 H_1 / A_1 A_1 \rightarrow b\bar{b}$ for lower masses. With increasingly higher DM masses, the contribution from the $b\bar{b}$ process decreases, while the decay to $W^{+*}W^{-*}$ becomes dominant. Near $m_{\text{DM}} \sim m_W$, the process $H_1 H_1 / A_1 A_1 \rightarrow W^+ W^-$ depletes the relic sharply, thus resulting in the observed steep boundary around this region. Direct detection constraints exclude larger values of g_1 , thereby limiting the coupling in this low-mass regime to be of order $\mathcal{O}(10^{-5})$. There is also an increase in difficulty when sampling points for $m_{\text{DM}} \lesssim m_h/2$ GeV, as this region is extremely constrained due to bounds from the 125 GeV Higgs boson invisible branching ratio, measured by the ATLAS experiment at $\text{BR}(h_{125} \rightarrow \text{invisible}) \leq 0.107 \pm 0.077$ [42].

For the intermediate mass region of $m_{\text{DM}} > m_W$ up until $m_{\text{DM}} \lesssim 380$ GeV, DM is under-produced due to the annihilation into gauge bosons. From this point upward, until our imposed scan upper mass $m_{\text{DM}} \leq 1000$ GeV, it is possible to account for the full relic in the entire mass range, while obeying every constraint, with a g_1 coupling of the order $\mathcal{O}(10^{-4})$, increasing with the DM mass.

B. Deviations from the $\theta = \frac{\pi}{4}$ alignment

Scanning the parameter space in the limit $\theta = \frac{\pi}{4}$ is a conservative choice, as it eliminates the term $ZH_i A_i \sim \cos(2\theta)$ that depletes the relic abundance. However, this does not imply one has to cancel this term exactly in order to obtain the correct relic. Therefore, we depart from this limit, allowing θ to acquire any possible value in its domain, $-\frac{\pi}{2} \leq \theta \leq \frac{\pi}{2}$.

The scanning process becomes much more computationally challenging, as it adds another dimension to the exploratory hyperplane and satisfying the relic abundance is difficult, with the additional depletion channel allowed. Given the strong constraints imposed, the prototype seed selection methods described in Section III B and detailed in App. B proved essential for achieving an efficient and comprehensive exploration of the parameter space.

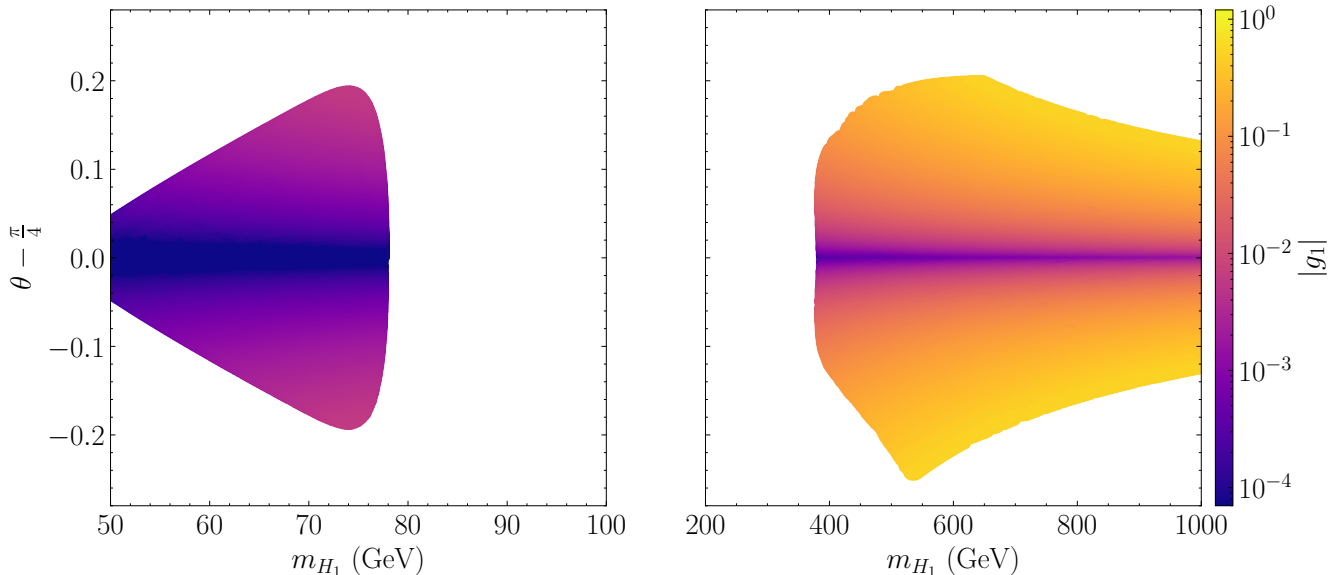


Figure 6: Scans with colour code for $|g_1|$. All theoretical constraints are applied, along with bounds from `HiggsTools`, direct detection and relic density. These points are sampled using *seeds* and *focus* on the parameters and observables of interest, deviating from the limit $\theta = \frac{\pi}{4}$.

In Fig. 6, we show our final results, with the allowed range of values for θ against the DM mass, with a color code for the DM-Higgs coupling g_1 . The y-axis is shifted by $\frac{\pi}{4}$ to emphasize the deviation from the conservative limit. The most striking feature at first glance is the allowed range of values for g_1 . For lower masses, by deviating from the θ limit, one can increase the maximum value found for g_1 by an order of magnitude, from $\mathcal{O}(10^{-5} \sim 10^{-4})$ to $\mathcal{O}(10^{-4} \sim 10^{-3})$. It is even more noticeable for the high mass region, as the increase spans over three orders of magnitude, from $\mathcal{O}(10^{-4})$ to $\leq \mathcal{O}(0.1)$. We found values up to the maximum allowed in our scans of $|g_1| \sim 0.5$.

We also see how the value of g_1 increases the further we stand from $\theta = \frac{\pi}{4}$. This happens as the main DM portal shifts from being the Higgs to the Z interaction. As long as one fulfils the relic requirements, along with the other strong limits on g_1 such as the direct detection bounds, it is possible to increase the value of the coupling.

For the low mass region, the shape of the allowed parameter space is strongly bounded by the relic constraint. It is possible to expand the values of θ for the lower masses to $|\theta - \frac{\pi}{4}| \lesssim 0.2$. The asymmetric shape on the high mass region results from a combination of the potential BFB conditions, relic constraint and direct detection limits, which are responsible for the oblique cuts on the plane. We found it possible to expand the values of θ for the high masses to $-0.26 \lesssim \theta - \frac{\pi}{4} \lesssim 0.2$.

VI. CONCLUSIONS

We have conducted a detailed study of a viable particle dark matter model with two mass-degenerate states of opposite CP quantum number, H_1 and A_1 . The SM is extended by two additional Higgs doublets, and a discrete \mathbb{Z}_3 symmetry acting on the three doublet fields ensures the stability of the dark matter states. Starting from the scalar potential, we reviewed the derivation of the potential parameters in terms of the independent parameters, including the physical masses in Eq.(13). We then proceeded to describe the theoretical consistency conditions that the model must satisfy, with the boundedness from below, global minimum and unitarity, as well as the relevant experimental constraints from existing searches.

To explore the parameter space of the model, we employed machine learning techniques capable of efficiently probing complex, high-dimensional BSM scenarios without requiring pre-existing training data. Specifically, we combined an

Evolutionary Strategy algorithm [61] with an anomaly-detection-based Novelty Reward mechanism [29] to identify phenomenologically viable points.

Our analysis was structured in three parts. First, we followed the approach of Ref. [25] by imposing the conservative limit $\theta = \frac{\pi}{4}$, which eliminates the $ZH_i A_i$ coupling (proportional to $\cos 2\theta$) capable of depleting the relic abundance. Within two benchmark scenarios defined by fixed differences between the physical masses, we successfully reproduced the previous results under the corresponding constraints. However, upon applying our more stringent theoretical consistency conditions, notably the boundedness from below, the scanned points were found to be excluded. This outcome highlights the critical importance of a robust analytical foundation in the study of BSM models.

We go beyond the literature by allowing all physical masses to vary freely within the scan range defined in Eq. (29), while retaining the conservative choice $\theta = \frac{\pi}{4}$. In this condition, we find that the relic abundance requirement can be satisfied simultaneously with all theoretical and experimental constraints, yielding two distinct allowed regions for the mass of the two degenerate DM states: a low-mass region $50 \text{ GeV} \lesssim m_{\text{DM}} \lesssim m_W$, and a high-mass region extending from $m_{\text{DM}} \gtrsim 380 \text{ GeV}$ up to the scan limit of 1000 GeV. This broadening of the viable spectrum on both ends is made possible by dedicated searches. In the intermediate mass region, DM is found to be under-produced due to the efficient annihilation into gauge bosons. The stringent direct detection constraints restrict the Higgs-DM coupling g_1 to values of order 10^{-5} in the low-mass region and 10^{-4} in the high-mass region. Notably, many of the viable points we identify still lie within the neutrino fog, where it presents an irreducible background. As a result, even next-generation direct detection experiments may not be able to definitively rule out the model.

Finally, we allow the DM mixing angle θ to vary freely across its full domain, $-\frac{\pi}{2} \leq \theta \leq \frac{\pi}{2}$. In this case, we find that agreement with all constraints can be achieved with significantly larger Higgs-DM couplings, reaching values as high as $|g_1| \sim 0.5$. The inclusion of θ as a free parameter substantially increases the computational demands of the scan, introducing an additional depletion channel that makes satisfying the relic abundance more challenging. To address this complexity, we develop density-based methods to automatically select prototype points that serve as seeds for subsequent scan runs, following the procedures introduced in Section IIIB and detailed in Appendix B. Future work will be directed toward quantifying the differences between the methods and use them to fully automate the scan pipeline. Another promising application of prototype selection lies in identifying benchmark parameter choices that maximize a specific signature for a given model. For example, those most likely to be probed at upcoming collider experiments or in next-generation direct detection DM searches.

ACKNOWLEDGMENTS

We thank João Paulo Silva for discussions. This work is supported in part by the Portuguese Fundação para a Ciência e Tecnologia (FCT) through the PRR (Recovery and Resilience Plan), within the scope of the investment “RE-C06-i06 - Science Plus Capacity Building”, measure “RE-C06-i06.m02 - Reinforcement of financing for International Partnerships in Science, Technology and Innovation of the PRR”, with a grant under the project with reference 2024.01362.CERN, and through Centro de Física Teórica de Partículas (CFTP) Contracts UIDB/00777/2020, and UIDP/00777/2020, partially funded through POCTI (FEDER), COMPETE, QREN, and the EU. The work of R.B. is supported by the Deutsche Forschungsgemeinschaft (DFG, German Research Foundation) under grant 396021762-TRR 257. MCR is supported by the STFC under Grant No. ST/T001011/1. F.A. de Souza is also supported by FCT under the research grant with reference No. UI/BD/153105/2022.

-
- [1] **ATLAS** Collaboration, G. Aad et al., *Observation of a new particle in the search for the Standard Model Higgs boson with the ATLAS detector at the LHC*, *Phys. Lett. B* **716** (2012) 1–29, [[arXiv:1207.7214](#)].
 - [2] **CMS** Collaboration, S. Chatrchyan et al., *Observation of a New Boson at a Mass of 125 GeV with the CMS Experiment at the LHC*, *Phys. Lett. B* **716** (2012) 30–61, [[arXiv:1207.7235](#)].
 - [3] **Planck** Collaboration, P. A. R. Ade et al., *Planck 2013 results. I. Overview of products and scientific results*, *Astron. Astrophys.* **571** (2014) A1, [[arXiv:1303.5062](#)].
 - [4] N. G. Deshpande and E. Ma, *Pattern of Symmetry Breaking with Two Higgs Doublets*, *Phys. Rev. D* **18** (1978) 2574.
 - [5] E. Ma, *Verifiable radiative seesaw mechanism of neutrino mass and dark matter*, *Phys. Rev. D* **73** (2006) 077301, [[hep-ph/0601225](#)].
 - [6] R. Barbieri, L. J. Hall, and V. S. Rychkov, *Improved naturalness with a heavy Higgs: An Alternative road to LHC physics*, *Phys. Rev. D* **74** (2006) 015007, [[hep-ph/0603188](#)].

- [7] L. Lopez Honorez, E. Nezri, J. F. Oliver, and M. H. G. Tytgat, *The Inert Doublet Model: An Archetype for Dark Matter*, *JCAP* **02** (2007) 028, [[hep-ph/0612275](#)].
- [8] E. Nezri, M. H. G. Tytgat, and G. Vertongen, *e^+ and anti- p from inert doublet model dark matter*, *JCAP* **04** (2009) 014, [[arXiv:0901.2556](#)].
- [9] C. Arina, F.-S. Ling, and M. H. G. Tytgat, *IDM and i IDM or The Inert Doublet Model and Inelastic Dark Matter*, *JCAP* **10** (2009) 018, [[arXiv:0907.0430](#)].
- [10] L. Lopez Honorez and C. E. Yaguna, *The inert doublet model of dark matter revisited*, *JHEP* **09** (2010) 046, [[arXiv:1003.3125](#)].
- [11] L. Lopez Honorez and C. E. Yaguna, *A new viable region of the inert doublet model*, *JCAP* **01** (2011) 002, [[arXiv:1011.1411](#)].
- [12] A. Arhrib, Y.-L. S. Tsai, Q. Yuan, and T.-C. Yuan, *An Updated Analysis of Inert Higgs Doublet Model in light of the Recent Results from LUX, PLANCK, AMS-02 and LHC*, *JCAP* **06** (2014) 030, [[arXiv:1310.0358](#)].
- [13] M. Klasen, C. E. Yaguna, and J. D. Ruiz-Alvarez, *Electroweak corrections to the direct detection cross section of inert higgs dark matter*, *Phys. Rev. D* **87** (2013) 075025, [[arXiv:1302.1657](#)].
- [14] A. Ilnicka, M. Krawczyk, and T. Robens, *Inert Doublet Model in light of LHC Run I and astrophysical data*, *Phys. Rev. D* **93** (2016), no. 5 055026, [[arXiv:1508.01671](#)].
- [15] A. Belyaev, G. Cacciapaglia, I. P. Ivanov, F. Rojas-Abatte, and M. Thomas, *Anatomy of the Inert Two Higgs Doublet Model in the light of the LHC and non-LHC Dark Matter Searches*, *Phys. Rev. D* **97** (2018), no. 3 035011, [[arXiv:1612.00511](#)].
- [16] B. Eiteneuer, A. Goudelis, and J. Heisig, *The inert doublet model in the light of Fermi-LAT gamma-ray data: a global fit analysis*, *Eur. Phys. J. C* **77** (2017), no. 9 624, [[arXiv:1705.01458](#)].
- [17] J. Kalinowski, W. Kotlarski, T. Robens, D. Sokolowska, and A. F. Zarnecki, *Benchmarking the Inert Doublet Model for e^+e^- colliders*, *JHEP* **12** (2018) 081, [[arXiv:1809.07712](#)].
- [18] A. Belyaev, T. R. Fernandez Perez Tomei, P. G. Mercadante, C. S. Moon, S. Moretti, S. F. Novaes, L. Panizzi, F. Rojas, and M. Thomas, *Advancing LHC probes of dark matter from the inert two-Higgs-doublet model with the monojet signal*, *Phys. Rev. D* **99** (2019), no. 1 015011, [[arXiv:1809.00933](#)].
- [19] A. Ilnicka, T. Robens, and T. Stefaniak, *Constraining Extended Scalar Sectors at the LHC and beyond*, *Mod. Phys. Lett. A* **33** (2018), no. 10n11 1830007, [[arXiv:1803.03594](#)].
- [20] S. Banerjee, F. Boudjema, N. Chakrabarty, G. Chalons, and H. Sun, *Relic density of dark matter in the inert doublet model beyond leading order: The heavy mass case*, *Phys. Rev. D* **100** (2019), no. 9 095024, [[arXiv:1906.11269](#)].
- [21] S. Banerjee, F. Boudjema, N. Chakrabarty, and H. Sun, *Relic density of dark matter in the inert doublet model beyond leading order for the low mass region: 1. Renormalisation and constraints*, *Phys. Rev. D* **104** (2021) 075002, [[arXiv:2101.02165](#)].
- [22] A. Ghosh, P. Konar, and S. Seth, *Precise probing of the inert Higgs-doublet model at the LHC*, *Phys. Rev. D* **105** (2022), no. 11 115038, [[arXiv:2111.15236](#)].
- [23] P. M. Ferreira and J. P. Silva, *Discrete and continuous symmetries in multi-Higgs-doublet models*, *Phys. Rev. D* **78** (2008) 116007, [[arXiv:0809.2788](#)].
- [24] M. P. Bento, H. E. Haber, J. C. Romão, and J. P. Silva, *Multi-Higgs doublet models: physical parametrization, sum rules and unitarity bounds*, *JHEP* **11** (2017) 095, [[arXiv:1708.09408](#)].
- [25] A. Aranda, D. Hernández-Otero, J. Hernández-Sánchez, V. Keus, S. Moretti, D. Rojas-Ciofalo, and T. Shindou, *Z_3 symmetric inert ($2+1$)-Higgs-doublet model*, *Phys. Rev. D* **103** (2021), no. 1 015023, [[arXiv:1907.12470](#)].
- [26] D. Das and I. Saha, *Alignment limit in three Higgs-doublet models*, *Phys. Rev. D* **100** (2019), no. 3 035021, [[arXiv:1904.03970](#)].
- [27] R. Boto, J. C. Romão, and J. P. Silva, *Current bounds on the type-Z Z_3 three-Higgs-doublet model*, *Phys. Rev. D* **104** (2021), no. 9 095006, [[arXiv:2106.11977](#)].
- [28] R. Boto, D. Das, L. Lourenco, J. C. Romao, and J. P. Silva, *Fingerprinting the type-Z three-Higgs-doublet models*, *Phys. Rev. D* **108** (2023), no. 1 015020, [[arXiv:2304.13494](#)].
- [29] J. C. Romão and M. Crispim Romão, *Combining evolutionary strategies and novelty detection to go beyond the alignment limit of the Z_3 3HDM*, *Phys. Rev. D* **109** (2024), no. 9 095040, [[arXiv:2402.07661](#)].
- [30] M. Chakraborti, D. Das, M. Levy, S. Mukherjee, and I. Saha, *Prospects for light charged scalars in a three-Higgs-doublet model with Z_3 symmetry*, *Phys. Rev. D* **104** (2021), no. 7 075033, [[arXiv:2104.08146](#)].
- [31] D. Das, M. Levy, P. B. Pal, A. M. Prasad, I. Saha, and A. Srivastava, *Democratic three-Higgs-doublet models: The custodial limit and wrong-sign Yukawa coupling*, *Phys. Rev. D* **107** (2023), no. 5 055035, [[arXiv:2301.00231](#)].
- [32] B. Coleppa, A. Khanna, and G. B. Krishna, *3HDM at the ILC*, [[arXiv:2506.24094](#)].
- [33] B. Coleppa, A. Khanna, S. K. Rai, and A. Sarkar, *LHC Signatures of Neutral Scalar Cascades in the Z_3 symmetric 3HDM*, [[arXiv:2601.15683](#)].
- [34] B. Coleppa, B. Fuks, and A. Khanna, *Flavour-Changing Neutral Current Top Decays in the Three Higgs Doublet Model*, [[arXiv:2601.16647](#)].
- [35] B. Coleppa and A. Khanna, *Neutral Scalar Signatures at a Muon Collider in the Z_3 symmetric Three Higgs Doublet Model*, [[arXiv:2602.17460](#)].
- [36] A. Cordero-Cid, J. Hernández-Sánchez, V. Keus, S. F. King, S. Moretti, D. Rojas, and D. Sokolowska, *CP violating scalar Dark Matter*, *JHEP* **12** (2016) 014, [[arXiv:1608.01673](#)].
- [37] A. Cordero, J. Hernandez-Sanchez, V. Keus, S. F. King, S. Moretti, D. Rojas, and D. Sokolowska, *Dark Matter Signals at the LHC from a 3HDM*, *JHEP* **05** (2018) 030, [[arXiv:1712.09598](#)].

- [38] J. Hernandez-Sanchez, V. Keus, S. Moretti, D. Rojas-Ciofalo, and D. Sokolowska, *Complementary Probes of Two-component Dark Matter*, [arXiv:2012.11621](#).
- [39] J. Hernandez-Sanchez, V. Keus, S. Moretti, and D. Sokolowska, *Complementary collider and astrophysical probes of multi-component Dark Matter*, *JHEP* **03** (2023) 045, [[arXiv:2202.10514](#)].
- [40] R. Boto, P. N. Figueiredo, J. C. Romão, and J. P. Silva, *Novel two component dark matter features in the $Z_2 \times Z_2$ 3HDM*, *Journal of High Energy Physics* **2024** (2024), no. 108.
- [41] **LZ** Collaboration, J. Aalbers et al., *Dark Matter Search Results from 4.2 Tonne-Years of Exposure of the LUX-ZEPLIN (LZ) Experiment*, *Phys. Rev. Lett.* **135** (2025), no. 1 011802, [[arXiv:2410.17036](#)].
- [42] **ATLAS** Collaboration, G. Aad et al., *Combination of searches for invisible decays of the Higgs boson using 139 fb⁻¹ of proton-proton collision data at $s=13$ TeV collected with the ATLAS experiment*, *Phys. Lett. B* **842** (2023) 137963, [[arXiv:2301.10731](#)].
- [43] **Planck** Collaboration, N. Aghanim et al., *Planck 2018 results. VI. Cosmological parameters*, *Astron. Astrophys.* **641** (2020) A6, [[arXiv:1807.06209](#)]. [Erratum: *Astron. Astrophys.* 652, C4 (2021)].
- [44] M. Gonçalves, M. Mühlleitner, R. Santos, and T. Trindade, *Dark Matter in Multi-Singlet Extensions of the Standard Model*, [arXiv:2505.07753](#).
- [45] M. Feickert and B. Nachman, *A Living Review of Machine Learning for Particle Physics*, [arXiv:2102.02770](#).
- [46] P. Shanahan et al., *Snowmass 2021 Computational Frontier CompF03 Topical Group Report: Machine Learning*, [arXiv:2209.07559](#).
- [47] T. Plehn, A. Butter, B. Dillon, T. Heimel, C. Krause, and R. Winterhalder, *Modern Machine Learning for LHC Physicists*, [arXiv:2211.01421](#).
- [48] J. M. Duarte, U. Seljak, and K. Terao, *Machine Learning*, [arXiv:2512.11133](#).
- [49] S. Caron, J. S. Kim, K. Rolbiecki, R. Ruiz de Austri, and B. Stienen, *The BSM-AI project: SUSY-AI-generalizing LHC limits on supersymmetry with machine learning*, *Eur. Phys. J. C* **77** (2017), no. 4 257, [[arXiv:1605.02797](#)].
- [50] S. Caron, T. Heskes, S. Otten, and B. Stienen, *Constraining the Parameters of High-Dimensional Models with Active Learning*, *Eur. Phys. J. C* **79** (2019), no. 11 944, [[arXiv:1905.08628](#)].
- [51] F. Staub, *xBIT: an easy to use scanning tool with machine learning abilities*, [arXiv:1906.03277](#).
- [52] B. S. Kronheim, M. P. Kuchera, H. B. Prosper, and A. Karbo, *Bayesian Neural Networks for Fast SUSY Predictions*, *Phys. Lett. B* **813** (2021) 136041, [[arXiv:2007.04506](#)].
- [53] J. Hollingsworth, M. Ratz, P. Tanedo, and D. Whiteson, *Efficient sampling of constrained high-dimensional theoretical spaces with machine learning*, *Eur. Phys. J. C* **81** (2021), no. 12 1138, [[arXiv:2103.06957](#)].
- [54] M. D. Goodsell and A. Joury, *Active learning BSM parameter spaces*, *Eur. Phys. J. C* **83** (2023), no. 4 268, [[arXiv:2204.13950](#)].
- [55] M. A. Diaz, G. Cerro, S. Dasmahapatra, and S. Moretti, *Bayesian Active Search on Parameter Space: a 95 GeV Spin-0 Resonance in the $(B-L)$ SSM*, [arXiv:2404.18653](#).
- [56] M. A. Diaz, S. Dasmahapatra, and S. Moretti, *hep-aid: A Python Library for Sample Efficient Parameter Scans in Beyond the Standard Model Phenomenology*, [arXiv:2412.17675](#).
- [57] S. AbdusSalam, S. Abel, and M. Crispim Romão, *Symbolic regression for beyond the standard model physics*, *Phys. Rev. D* **111** (2025), no. 1 015022, [[arXiv:2405.18471](#)].
- [58] N. Batra, B. Coleppa, A. Khanna, S. K. Rai, and A. Sarkar, *Constraining the 3HDM Parameter Space*, [arXiv:2504.07489](#).
- [59] A. Hammad, R. Ramos, A. Chakraborty, P. Ko, and S. Moretti, *Explaining Data Anomalies over the NMSSM Parameter Space with Deep Learning Techniques*, [arXiv:2508.13912](#).
- [60] T. Biekötter, *evortran: a modern Fortran package for genetic algorithms with applications from LHC data fitting to LISA signal reconstruction*, [arXiv:2507.06082](#).
- [61] F. A. de Souza, M. Crispim Romão, N. F. Castro, M. Nikjoo, and W. Porod, *Exploring parameter spaces with artificial intelligence and machine learning black-box optimization algorithms*, *Phys. Rev. D* **107** (2023), no. 3 035004, [[arXiv:2206.09223](#)].
- [62] F. S. Faro and I. P. Ivanov, *Boundedness from below in the $U(1) \times U(1)$ three-Higgs-doublet model*, *Phys. Rev. D* **100** (2019), no. 3 035038, [[arXiv:1907.01963](#)].
- [63] R. Boto, J. C. Romão, and J. P. Silva, *Bounded from below conditions on a class of symmetry constrained 3HDM*, *Phys. Rev. D* **106** (2022), no. 11 115010, [[arXiv:2208.01068](#)].
- [64] K. G. Klimenko, *On Necessary and Sufficient Conditions for Some Higgs Potentials to Be Bounded From Below*, *Theor. Math. Phys.* **62** (1985) 58–65.
- [65] K. Kannike, *Vacuum Stability Conditions From Copositivity Criteria*, *Eur. Phys. J. C* **72** (2012) 2093, [[arXiv:1205.3781](#)].
- [66] R. F. T. Boto, *Constraining Multi-scalars models with colliders and Dark Matter*. PhD thesis, IST, Lisbon (main), 2025. [arXiv:2509.19004](#).
- [67] F. James and M. Roos, *Minuit: A System for Function Minimization and Analysis of the Parameter Errors and Correlations*, *Comput. Phys. Commun.* **10** (1975) 343–367.
- [68] A. Pierce and J. Thaler, *Natural Dark Matter from an Unnatural Higgs Boson and New Colored Particles at the TeV Scale*, *JHEP* **08** (2007) 026, [[hep-ph/0703056](#)].
- [69] F. A. de Souza, N. F. Castro, M. Crispim Romão, and W. Porod, *Exploring scotogenic parameter spaces and mapping uncharted dark matter phenomenology with multi-objective search algorithms*, *JHEP* **10** (2025) 116, [[arXiv:2505.08862](#)].

- [70] F. A. de Souza, R. Boto, M. Crispim Romão, P. N. Figueiredo, J. C. Romão, and J. P. Silva, *Unearthing large pseudoscalar Yukawa couplings with machine learning*, *JHEP* **07** (2025) 268, [[arXiv:2505.10625](#)].
- [71] R. Boto, T. P. Rebelo, J. C. Romão, and J. P. Silva, *Machine Learning in the 2HDM2S model for Dark Matter*, [arXiv:2509.01677](#). [arXiv:2509.01677](#).
- [72] R. Boto, J. A. C. Matos, J. C. Romão, and J. P. Silva, *Surveying the complex three Higgs doublet model with Machine Learning*, [arXiv:2510.02445](#).
- [73] R. Boto, K. Elyauti, D. Fontes, M. Gonçalves, M. Mühlleitner, J. C. Romão, R. Santos, and J. P. Silva, *Reassessing CP Violation in the C2HDM with Machine Learning*, [arXiv:2601.15227](#).
- [74] H. Bahl, T. Biekötter, S. Heinemeyer, C. Li, S. Paasch, G. Weiglein, and J. Wittbrodt, *HiggsTools: BSM scalar phenomenology with new versions of HiggsBounds and HiggsSignals*, *Comput. Phys. Commun.* **291** (2023) 108803, [[arXiv:2210.09332](#)].
- [75] G. Alguero, G. Belanger, F. Boudjema, S. Chakraborti, A. Goudelis, S. Kraml, A. Mjallal, and A. Pukhov, *micrOMEGAs 6.0: N-component dark matter*, *Comput. Phys. Commun.* **299** (2024) 109133, [[arXiv:2312.14894](#)].
- [76] N. Hansen and A. Ostermeier, *Adapting arbitrary normal mutation distributions in evolution strategies: The covariance matrix adaptation*, pp. 312 – 317, **06**, 1996.
- [77] N. Hansen and A. Ostermeier, *Completely derandomized self-adaptation in evolution strategies*, *Evolutionary Computation* **9** (2001), no. 2 159–195.
- [78] N. Hansen, *The cma evolution strategy: A tutorial*, [arXiv:1604.00772](#). [arXiv:1604.00772](#).
- [79] M. Nomura and M. Shibata, *cmaes : A simple yet practical python library for cma-es*, [arXiv:2402.01373](#). [arXiv:2402.01373](#).
- [80] M. Goldstein and A. Dengel, *Histogram-based outlier score (hbos): A fast unsupervised anomaly detection algorithm*, . [Available online](#).
- [81] H.-P. Kriegel, P. Kröger, E. Schubert, and A. Zimek, *Loop: local outlier probabilities*, in *Proceedings of the 18th ACM Conference on Information and Knowledge Management, CIKM '09*, (New York, NY, USA), pp. 1649–1652, Association for Computing Machinery, 2009.
- [82] A. Guryanov, *Histogram-based algorithm for building gradient boosting ensembles of piecewise linear decision trees*, in *Analysis of Images, Social Networks and Texts: 8th International Conference, AIST 2019, Kazan, Russia, July 17–19, 2019, Revised Selected Papers*, (Berlin, Heidelberg), p. 39–50, Springer-Verlag, 2019.
- [83] D. Sculley, *Web-scale k-means clustering*, in *Proceedings of the 19th International Conference on World Wide Web, WWW '10*, (New York, NY, USA), p. 1177–1178, Association for Computing Machinery, 2010.
- [84] M. M. Breunig, H.-P. Kriegel, R. T. Ng, and J. Sander, *Lof: identifying density-based local outliers*, *SIGMOD Rec.* **29** (May, 2000) 93–104.
- [85] M. C. Peixoto, N. F. Castro, M. Crispim Romão, M. G. J. Oliveira, and I. Ochoa, *Fitting a collider in a quantum computer: tackling the challenges of quantum machine learning for big datasets*, *Front. Artif. Intell.* **6** (2023) 1268852, [[arXiv:2211.03233](#)].
- [86] S. Moretti and K. Yagyu, *Constraints on Parameter Space from Perturbative Unitarity in Models with Three Scalar Doublets*, *Phys. Rev. D* **91** (2015) 055022, [[arXiv:1501.06544](#)].
- [87] M. P. Bento, J. C. Romão, and J. P. Silva, *Unitarity bounds for all symmetry-constrained 3HDMs*, *JHEP* **08** (2022) 273, [[arXiv:2204.13130](#)].
- [88] **Gfitter Group** Collaboration, M. Baak, J. Cúth, J. Haller, A. Hoecker, R. Kogler, K. Mönig, M. Schott, and J. Stelzer, *The global electroweak fit at NNLO and prospects for the LHC and ILC*, *Eur. Phys. J. C* **74** (2014) 3046, [[arXiv:1407.3792](#)].
- [89] W. Grimus, L. Lavoura, O. M. Ogreid, and P. Osland, *The Oblique parameters in multi-Higgs-doublet models*, *Nucl. Phys. B* **801** (2008) 81–96, [[arXiv:0802.4353](#)].
- [90] **ATLAS** Collaboration, G. Aad et al., *A detailed map of Higgs boson interactions by the ATLAS experiment ten years after the discovery*, *Nature* **607** (2022), no. 7917 52–59, [[arXiv:2207.00092](#)]. [Erratum: *Nature* 612, E24 (2022)].
- [91] **Particle Data Group** Collaboration, S. Navas et al., *Review of particle physics*, *Phys. Rev. D* **110** (2024), no. 3 030001.
- [92] J. Heisig, S. Kraml, and A. Lessa, *Constraining new physics with searches for long-lived particles: Implementation into SModelS*, *Phys. Lett. B* **788** (2019) 87–95, [[arXiv:1808.05229](#)].
- [93] D. Fontes and J. C. Romão, *FeynMaster: a plethora of Feynman tools*, *Comput. Phys. Commun.* **256** (2020) 107311, [[arXiv:1909.05876](#)].
- [94] D. Fontes and J. C. Romão, *Renormalization of the C2HDM with FeynMaster 2*, *JHEP* **06** (2021) 016, [[arXiv:2103.06281](#)]. [Erratum: *JHEP* 12, 005 (2021)].
- [95] D. Fontes and J. C. Romão, *FeynMaster Manual*, [arXiv:2504.01865](#). [arXiv:2504.01865](#).
- [96] N. D. Christensen and C. Duhr, *FeynRules - Feynman rules made easy*, *Comput. Phys. Commun.* **180** (2009) 1614–1641, [[arXiv:0806.4194](#)].
- [97] A. Alloul, N. D. Christensen, C. Degrande, C. Duhr, and B. Fuks, *FeynRules 2.0 - A complete toolbox for tree-level phenomenology*, *Comput. Phys. Commun.* **185** (2014) 2250–2300, [[arXiv:1310.1921](#)].
- [98] P. Nogueira, *Automatic Feynman Graph Generation*, *J. Comput. Phys.* **105** (1993) 279–289.
- [99] R. Mertig, M. Bohm, and A. Denner, *FEYN CALC: Computer algebraic calculation of Feynman amplitudes*, *Comput. Phys. Commun.* **64** (1991) 345–359.
- [100] V. Shtabovenko, R. Mertig, and F. Orellana, *New Developments in FeynCalc 9.0*, *Comput. Phys. Commun.* **207** (2016) 432–444, [[arXiv:1601.01167](#)].

- [101] V. Shtabovenko, R. Mertig, and F. Orellana, *FeynCalc 9.3: New features and improvements*, *Comput. Phys. Commun.* **256** (2020) 107478, [[arXiv:2001.04407](#)].
- [102] **XLZD** Collaboration, J. Aalbers et al., *The XLZD Design Book: Towards the Next-Generation Liquid Xenon Observatory for Dark Matter and Neutrino Physics*, [arXiv:2410.17137](#). [arXiv:2410.17137](#).
- [103] C. A. J. O'Hare, *New Definition of the Neutrino Floor for Direct Dark Matter Searches*, *Phys. Rev. Lett.* **127** (2021), no. 25 251802, [[arXiv:2109.03116](#)].
- [104] G. Bélanger, K. Kannike, A. Pukhov, and M. Raidal, *Minimal semi-annihilating \mathbb{Z}_N scalar dark matter*, *JCAP* **06** (2014) 021, [[arXiv:1403.4960](#)].
- [105] **XENON** Collaboration, E. Aprile et al., *WIMP Dark Matter Search Using a 3.1 Tonne-Year Exposure of the XENONnT Experiment*, *Phys. Rev. Lett.* **135** (2025), no. 22 221003, [[arXiv:2502.18005](#)].
- [106] **PandaX** Collaboration, Z. Bo et al., *Dark Matter Search Results from 1.54 Tonne-Year Exposure of PandaX-4T*, *Phys. Rev. Lett.* **134** (2025), no. 1 011805, [[arXiv:2408.00664](#)].
- [107] **DarkSide-20k** Collaboration, C. E. Aalseth et al., *DarkSide-20k: A 20 tonne two-phase LAr TPC for direct dark matter detection at LNGS*, *Eur. Phys. J. Plus* **133** (2018) 131, [[arXiv:1707.08145](#)].
- [108] **Fermi-LAT** Collaboration, M. Ackermann et al., *Searching for Dark Matter Annihilation from Milky Way Dwarf Spheroidal Galaxies with Six Years of Fermi Large Area Telescope Data*, *Phys. Rev. Lett.* **115** (2015), no. 23 231301, [[arXiv:1503.02641](#)].
- [109] G. Belanger, A. Mjallal, and A. Pukhov, *Two dark matter candidates: The case of inert doublet and singlet scalars*, *Phys. Rev. D* **105** (2022), no. 3 035018, [[arXiv:2108.08061](#)].
- [110] **AMS** Collaboration, M. Aguilar et al., *Antiproton Flux, Antiproton-to-Proton Flux Ratio, and Properties of Elementary Particle Fluxes in Primary Cosmic Rays Measured with the Alpha Magnetic Spectrometer on the International Space Station*, *Phys. Rev. Lett.* **117** (2016), no. 9 091103.
- [111] **AMS** Collaboration, M. Aguilar et al., *Precision Measurement of the Boron to Carbon Flux Ratio in Cosmic Rays from 1.9 GV to 2.6 TV with the Alpha Magnetic Spectrometer on the International Space Station*, *Phys. Rev. Lett.* **117** (2016), no. 23 231102.
- [112] A. Reinert and M. W. Winkler, *A Precision Search for WIMPs with Charged Cosmic Rays*, *JCAP* **01** (2018) 055, [[arXiv:1712.00002](#)].
- [113] **H.E.S.S.** Collaboration, H. Abdalla et al., *Search for Dark Matter Annihilation Signals in the H.E.S.S. Inner Galaxy Survey*, *Phys. Rev. Lett.* **129** (2022), no. 11 111101, [[arXiv:2207.10471](#)].
- [114] **DARWIN** Collaboration, J. Aalbers et al., *DARWIN: towards the ultimate dark matter detector*, *JCAP* **11** (2016) 017, [[arXiv:1606.07001](#)].
- [115] J. Billard, L. Strigari, and E. Figueroa-Feliciano, *Implication of neutrino backgrounds on the reach of next generation dark matter direct detection experiments*, *Phys. Rev. D* **89** (2014), no. 2 023524, [[arXiv:1307.5458](#)].
- [116] C. A. J. O'Hare, *Can we overcome the neutrino floor at high masses?*, *Phys. Rev. D* **102** (2020), no. 6 063024, [[arXiv:2002.07499](#)].
- [117] Y. Freund and R. E. Schapire, *A Decision-Theoretic Generalization of On-Line Learning and an Application to Boosting*, *J. Comput. Syst. Sci.* **55** (1997), no. 1 119–139.
- [118] L. Breiman, *Prediction games and arcing algorithms*, *Neural Computation* **11** (10, 1999) 1493–1517.
- [119] J. Friedman, *Greedy function approximation: A gradient boosting machine*, *The Annals of Statistics* **29** (11, 2000).

Appendix A: Contributions to $\langle\sigma v\rangle$

We expected the same contribution from both DM components, H_1 and A_1 , to the relic density. This can only be achieved with the appropriate method to calculate the relic, as explained in IV B 1, due to the processes of co-scattering of the form $\text{DM SM} \rightarrow \text{DM}' \text{SM}'$ included only in that method.

In Fig. 7, we show the top contributions to the thermally-averaged cross-section times velocity, $\langle\sigma v\rangle$, with the expanding universe, presented as a function of the temperature, T . To follow the time evolution, t , of the universe, the plots should be read from right to left, since $T \propto t^{-1}$.

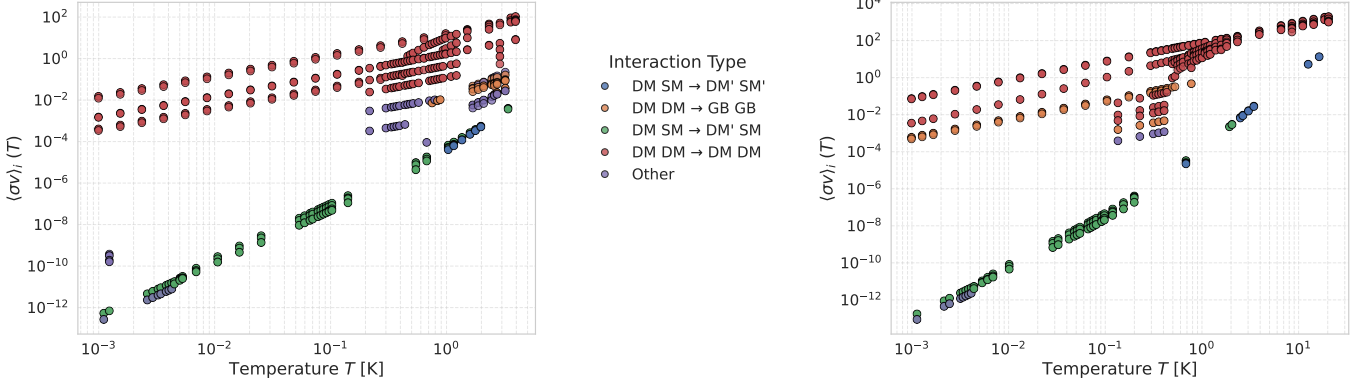


Figure 7: Processes contributing to $\langle\sigma v\rangle$ for $m_{H_1} = 70$ GeV on the left and $m_{H_1} = 400$ GeV on the right, as a function of the temperature of the Universe. The legend distinguishes points based on the interaction type, either with DM species, gauge bosons (GB) and other SM particles. Co-scattering processes such as $H_2^- u \rightarrow d H_1$, represented in the legend with the form $\text{DM SM} \rightarrow \text{DM}' \text{SM}'$, are relevant at high temperatures and contribute to deplete the relic.

From both plots, we can conclude that the processes of co-scattering, displayed mainly in pink and purple lines, are more relevant for higher temperatures, and become increasingly less effective as the universe cools down. They are essential to preserve balance between the DM candidates and to obtain the correct relic, as it tends to drop significantly when including more processes. If the contributions of such processes are not included, one might expect to get the correct relic when in fact, it is under-abundant, as $\langle\sigma v\rangle \propto \Omega^{-1}$ for freeze-out.

Appendix B: Prototype Selection Methods

Here we present the implementation details of the seed selection methods listed in Section III B. Specifically, we develop methods to automatically identify regions of the parameter space that warrant further exploration by employing multiple, distinct techniques, each characterised by its own strengths and limitations, thereby providing complementary approaches.

1. Seed selection with HGBC in sparse regions

The process of extracting seeds can be performed automatically with a machine learning classifier. For this work, we employed a Gradient Boosting (GB) algorithm [117–119], that uses decision trees as predictors. A GB builds an ensemble of decision trees which are sequentially fit on the residual errors made of the previous one. In this work, we employ a variation of GB known as Histogram-Based Gradient Boosting [82]. Namely, we use the Histogram Gradient Boosting Classifier (HGBC), that works by binning input features and replacing them with integers. With this implementation, it is possible to use more memory-efficient data-structures and it removes the need for sorting the features when training each tree. As a trade-off, binning causes some precision loss that ends up acting as a regularizer, either reducing overfitting or causing some underfitting. In our scenario, this proves useful, as we want to select a representative sample from the various regions that may need seeds, and not necessarily collect a large sample from one specific region.

Here, we provide examples of how HGBC can be used for seed selection. It is trained to distinguish the data from overlapping random noise. Given that HGBC has achieved an acceptable performance in its classification task, we

can then select some points to be used as seeds, typically 1% or less from the most outlying quantile in the data. In practice, a sizeable amount of training data is required in order to achieve an acceptable classification performance. Thus, this method is best used after a sufficiently large number of valid points have already been obtained by CMA-ES.

To exemplify the use of the HGBC, in Fig. 8 we show a plane originating from initial runs, covered by noise data points, and the result of the selection on the right. In this case, we are keeping only the 0.001% of points that are harder to distinguish from the uniform background. As we can see, this technique is especially capable of identifying regions of global lower density, where the user might want to focus further exploration.

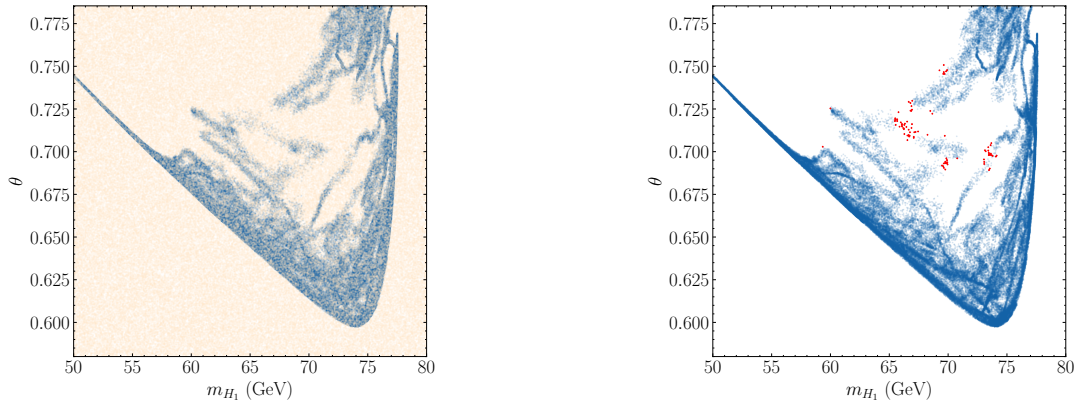


Figure 8: On the left, the uniform noise mask overlapped with data to train HGBC. On the right, points selected from the least dense regions in red.

2. Data Clustering using Mini-Batch k -Means

An early challenge encountered in this work was the generation of very large datasets of valid points. While this outcome attests to the effectiveness of the exploration methodology employed herein, it introduces substantial difficulties for subsequent data analysis and for the selection of new points to serve as seeds for additional runs. To address this issue, we employed a clustering algorithm to identify representative prototypes from the collected dataset of valid points, which were then used in downstream analysis and for seed selection. To this effect, we considered Mini-Batch k -Means (MBKM), a more efficient variation of the clustering algorithm k -Means which divides the full dataset into separate groups of equal variance, called clusters, while minimising a quantity known as the inertia. The inertia is simply the mean squared distance between each instance and its corresponding centroid, the cluster mean. MBKM uses batches instead of the full dataset, slightly adjusting the cluster centroids at each iteration while being much faster than regular k -Means. For our purposes, clustering the collection of amassed valid points comes with two applications.

A first application for MBKM is data condensation. Once the collection of valid points has grown considerably large ($\gtrsim 10^6$ points) the data analysis can start to become unpractical. In that case, it becomes useful to employ MBKM to provide a representation of the data around each cluster, reducing its size while maintaining the density distribution. On Fig. 9, we show how MBKM can be used to extract a representative sample of points from the dataset. We train MBKM with a large number of clusters. Notice how denser regions tend to form more compact clusters, with smaller radii. Then, one can simply collect the nearest points to the cluster centroids and use them to represent the dataset efficiently for further analysis.

A second application for MBKM is for seed selection, as points which lie furthest away from their corresponding centroids can be good candidates for seeds, since they are the least representative, or most outlier points from the clusters. This way, future CMA-ES scans using seeds from MBKM can work as effectively expanding the boundaries of the corresponding clusters. On Fig. 10, we show how we can select seeds using MBKM. This can be done either by hand-picking the clusters we are interested in or done automatically, by selecting the N clusters with higher radius. These can be combined to yield the desired results. Moreover, to restrict the selection to certain areas of the parameter space, it is possible to apply a user-defined rule that forces selection to a specific region of interest. It is important to note that in order to get the desired effect from MBKM, one needs to properly scale the data, for example with the Standard Scaler method, as to avoid directional biases during clustering.

Unlike HGBC, MBKM is a unsupervised learning technique, and so it is not limited to the amount of valid points

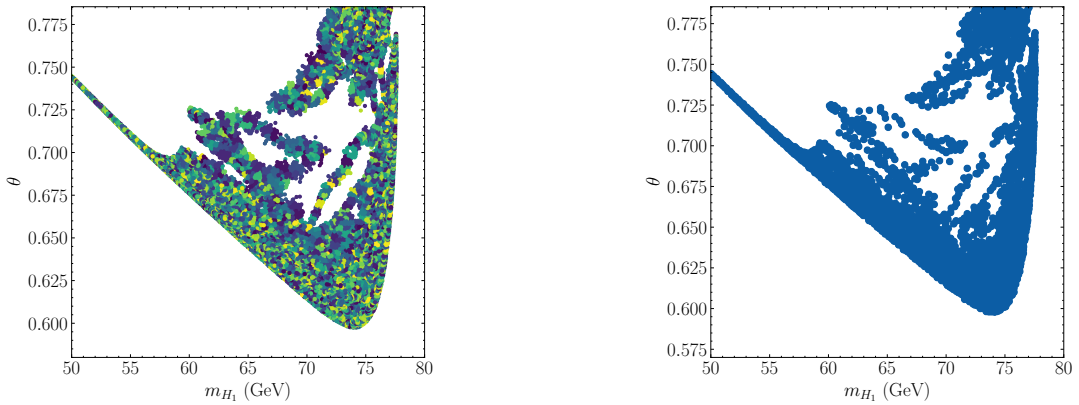


Figure 9: On the left, the clusters defined by MBKM. In this case, as MBKM is being used for sampling, we define a large number of clusters. On the right, the results of the sampling by selecting points near the cluster centroids.

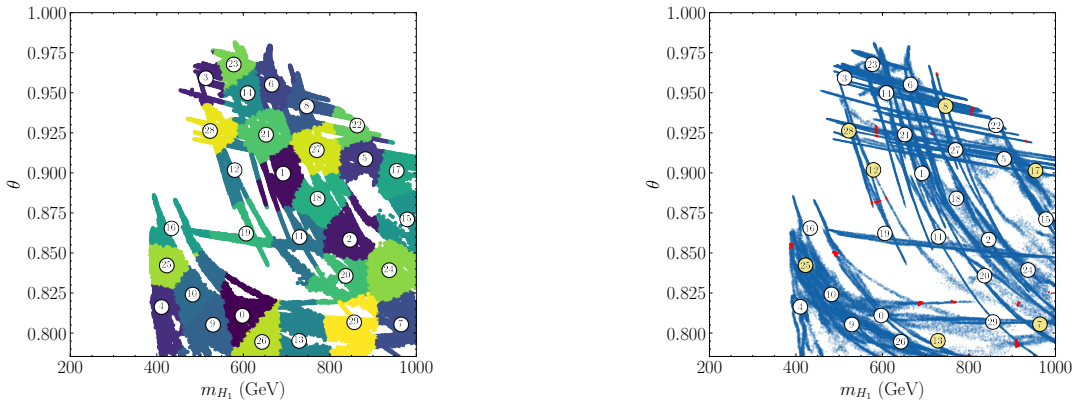


Figure 10: On the left, the results from applying MBKM clustering for seed selection. On the right, the points in red are extracted from selecting the clusters 7, 8, 12, 13, 17, 25 and 28, highlighted in yellow, and isolating the ones that lay furthest from their respective centroids.

amassed. However, MBKM assumes similar size, similar density and spherical shapes among clusters, which is not always the case, as can be seen for example with clusters 16 and 19 on Fig. 10. Additionally, the number of clusters needs to be specified as an input parameter, which can make automatization difficult for seed selection.

3. Seed selection with Local Outlier Factor

A third approach to automatically identify promising seeds used in this work was to use Local Outlier Factor (LOF). LOF is an algorithm specifically designed for outlier detection. Thus, its implementation is more straightforward than the two previous methods for seed selection. It works by identifying instances with local density that deviate significantly from their k -nearest neighbours. This way, it excels in isolating local outliers which are suitable to be used as seeds for CMA-ES. The $\sim 1\%$ most outlying valid points are good candidates for seeds. Unlike HGBC, LOF is a unsupervised learning technique, does not require a large training data and does not require a uniform background. Unlike MBKM, LOF does not assume a specific shape for its local neighbourhoods. The number of neighbours needs to be specified by the user, however $k = 20$ neighbours usually works well.

4. Complementary seed selection methods

In order to demonstrate how the three methods – HGBC, MBKM, and LOF – differ, we performed a comparative analysis among them. An illustrative example is provided in Fig. 11. For a fair comparison, each method is trained/fitted in the same set of points. These points were obtained from the scans with $\theta \geq \frac{\pi}{4}$ and novelty reward focus on m_{H_1}

and θ . The scores are normalised using a quantile transformation with a Gaussian distribution where the seeds are to be selected from amongst the points with the higher score values. The points which represent the 1% highest scoring quantile for each seed selection method are shown in Fig. 12.

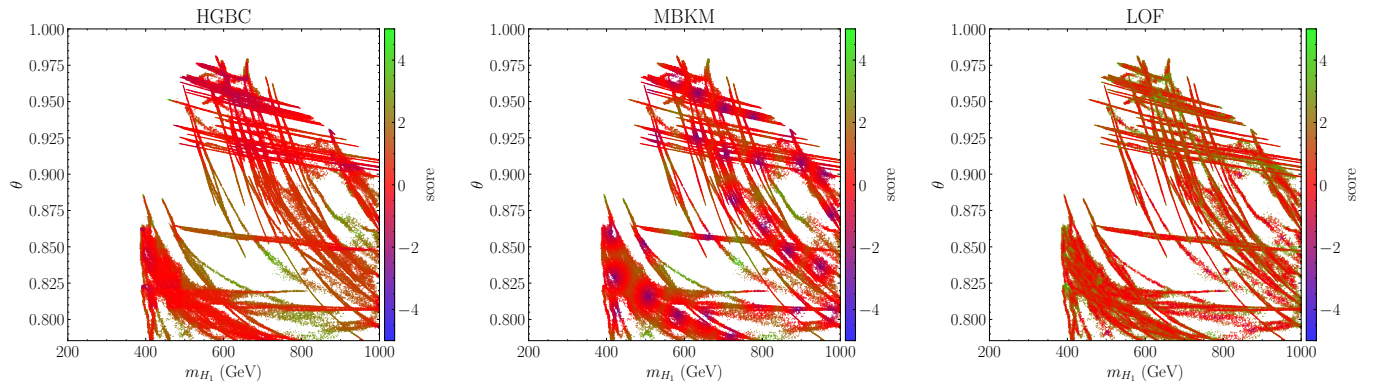


Figure 11: Comparison between three different seed selection methods: HGBC (left), MBKM (center), and LOF (right). The points are colour coded by the score given by each method. For ease of comparison, the scores are normalised by a quantile transformation with a Gaussian distribution. The seeds are to be selected amongst the highest scoring (green) points.

For HGBC a higher score is associated with points which are harder to distinguish from random noise. We can see in Fig. 11 the red-coloured horizontal and vertical slices corresponding to the tree partitions of the classifier containing the points which the classifier can easily isolate from the random noise. Whereas the green points with a higher score are harder to isolate from random noise with these tree partitions. This way, HGBC tends to prefer seeds in uniformly distributed and isolated areas, representing globally sparse regions, as shown in the left plot of Fig. 12.

For MBKM high scored points are the ones that lie furthest away from their cluster centroid. The colour pattern in Fig. 11 clearly show this behaviour, where the blue points are the ones closer to the centroids, while the green ones are the farthest and the ones which the seeds ought to be selected from. Being so, this method can often select seeds that lie in the frontier of clustered regions and the intersection between them. This can be seen in the central plot in Fig. 12.

LOF gives a higher score for points with a lower local density in a given neighbourhood. The colour pattern in Fig. 11 confirms this strategy where the red points corresponds to inlier points in the local neighbourhood and the green points the outliers ones. Thus, LOF typically selects seeds amongst points lying in the frontier of these neighbourhoods and the intersection between them, corresponding to locally underdense regions, as illustrated in the right plot in Fig. 12.

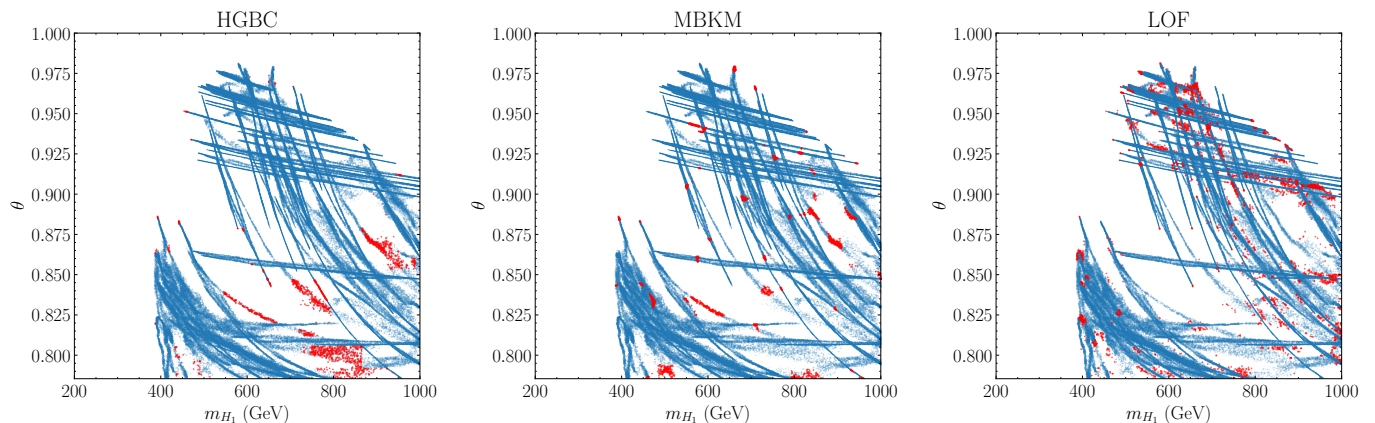


Figure 12: Comparison between three different seed selection methods: HGBC (left), MBKM (center), and LOF (right). The red points represent the 1% quantile with the highest scored points for each method.

Comparing the seeds selected from each method in Fig. 12 it is clear that HGBC, while excelling in isolating points in globally sparse regions, indicated in red on the left plot, it struggles to identify points in highly populated areas which are surrounded by completely empty regions. We can see this explicitly for the points that lie in the stripe patterns with $\theta \gtrsim 0.9$ which HGBC fails to target. However as indicated by the middle and right plots in Fig. 12,

LOF is able to target points in this region due to its k -neighbours algorithm focus on locality, that is absence in the HGBC case. MBKM enables the selection of specific regions of interest, which, when combined with parameter space scan rules to drive exploration, allows for a very efficient and targeted probing of the desired areas. If the goal is to efficiently and broadly populate the empty regions between the aforementioned stripes, LOF appears to be the most suitable choice. Finally, we can say the methods are complementary and seem to cover different use cases (global and local outliers) for targetting different interesting regions.